Oscillation-driven memory encoding, maintenance and recall in an entorhinal-hippocampal circuit model — Source link ⧉

Tomoki Kurikawa, Kenji Mizuseki, Tomoki Fukai

Institutions: Kansai Medical University, Osaka City University, Okinawa Institute of Science and Technology

Related papers:

- Oscillation-Driven Memory Encoding, Maintenance, and Recall in an Entorhinal–Hippocampal Circuit Model

- Developing a hippocampal neural prosthetic to facilitate human memory encoding and recall

- Theta coordinated error-driven learning in the hippocampus.

- Theta theory: Requirements for encoding events and task rules explain theta phase relationships in hippocampus and neocortex

- Exploration of the Neurobiological Basis for a Three-System, Multiattribute Model of Memory

1 **Title :**

2 **Oscillation-driven memory encoding, maintenance and recall in an**

3 **entorhinal-hippocampal circuit model**

4

5 **Authors**

6 Tomoki Kurikawa[1], Kenji Mizuseki[2], and Tomoki Fukai[3,4]

7

8 1. Department of Physics, Kansai Medical University, Hirakata, Osaka 573-1191, Japan

9 2. Department of Physiology, Osaka City University Graduate School of Medicine,
10 Abeno-ku, Osaka, 545-8585, JAPAN
11 3. Okinawa Institute of Science and Technology, Onna-son, Okinawa 904-0495, Japan

12 4. RIKEN Center for Brain Science, Wako, Saitama 351-0198, Japan

13

14   **Summary**

15   **During the execution of working memory tasks, task-relevant information is processed**

16   **by local circuits across multiple brain regions. How this multi-area computation is**

17   **conducted by the brain remains largely unknown. To explore such mechanisms in**

18   **spatial working memory, we constructed a neural network model involving**

19   **parvalbumin-positive, somatostatin-positive and vasoactive intestinal polypeptide-**

20   **positive interneurons in the hippocampal CA1 and the superficial and deep layers of**

21   **medial entorhinal cortex (MEC). Our model is based on a hypothesis that cholinergic**

22   **modulations differently regulate information flows across CA1 and MEC at memory**

23   **encoding, maintenance and recall during delayed nonmatching-to-place tasks. In the**

24   **model, theta oscillation coordinates the proper timing of interactions between these**

25   **regions. Furthermore, the model predicts that MEC is engaged in decoding as well as**

26   **encoding spatial memory, which we confirmed by experimental data analysis. Thus,**

27   **our model accounts for the neurobiological characteristics of the cross-area**

28   **information routing underlying working memory tasks.**

29

30   Keywords

31   Hippocampal CA1, Entorhinal cortex, theta oscillation, cross-area communications,

32   spatial working memory, disinhibitory circuit, cholinergic modulations

33

2

Introduction

Spatial navigation is a fundamental cognitive function that requires the processing of spatial memory by the hippocampus and entorhinal cortex. During a spatial navigation task, spatial information relevant to the task has to be encoded into, maintained in and recalled from spatial working memory at behaviorally adequate times. How these operations are coordinated by the cortico-hippocampal neural circuits during a spatial working memory task has yet to be explored.

A spatial working memory task is processed by several cortical areas such as the medial prefrontal cortex (mPFC) (Benchenane et al., 2010; Jones & Wilson, 2005; Spellman et al., 2015), medial entorhinal cortex (MEC)(Suh, Rivest, Nakashiba, Tominaga, & Tonegawa, 2011; Yamamoto, Suh, Takeuchi, & Tonegawa, 2014) and the hippocampal area CA1 (Benchenane et al., 2010). These anatomically connected areas (Eichenbaum, 2017; Swanson & Cowan, 1977; Witter, Wouterlood, Naber, & Van Haeften, 2000) are thought to mutually communicate information necessary to accomplish the task. Importantly, the degree of functional importance of different inter-area connections varies during the task. This is indicated by the fact that the impairment of these connections at different behavioral phases differentially influences task performance (Spellman et al., 2015; Suh et al., 2011; Yamamoto et al., 2014). For instance, in a delayed nonmatching to place task (DNMP), the maintenance of spatial memory during a delay period does not require synaptic connections from the layer 3 of the MEC (MECIII) to CA1, but these connections are necessary for memory recall (Yamamoto et al., 2014). Connections from CA1 to the mPFC play a crucial role in memory encoding but not in memory recall (Spellman et al., 2015). These results indicate that information flows via the hippocampal circuit are not static but are dynamically regulated depending on the behavioral demands.

Dynamic information routing across multiple areas is thought to reflect in coherence in neuronal activity between different areas (Spellman et al., 2015; Yamamoto et al., 2014), which leads to the hypothesis called "communication through coherence"(Fries, 2015).

64   Many theoretical (Akam & Kullmann, 2010; Buehlmann & Deco, 2010; Palmigiano,

65   Geisel, Wolf, & Battaglia, 2017; Vogels & Abbott, 2005; Yang, Murray, & Wang, 2016)

66   and experimental (Letzkus, Wolff, & Lüthi, 2015; Womelsdorf, Valiante, Sahin, Miller, &

67   Tiesinga, 2014) studies have explored the gating functions for this dynamic processing.

68   However, how the computations installed at multiple cortical areas are integrated to

69   execute a spatial working memory task including different cognitive stages (encoding,

70   maintenance, and decoding) remains largely unclear.

71

72   Here, we elucidated the underlying mechanisms of multi-area dynamic information

73   processing during DNMP tasks. We hypothesize that acetylcholine (ACh) controls spatial

74   information flows in the entorhinal-hippocampal circuit according to different cognitive

75   demands. Indeed, ACh is involved in diverse cognitive functions (Hasselmo & Sarter,

76   2010; Parikh, Kozak, Martinez, & Sarter, 2007) including fear conditioning (Letzkus et al.,

77   2011; Pi et al., 2013), sensory discrimination (Hangya, Ranade, Lorenc, & Kepecs, 2015;

78   Pinto et al., 2013), associative memory (Sabec, Wonnacott, Warburton, & Bashir, 2018),

79   and spatial (Croxson, Kyriazis, & Baxter, 2011; Okada, Nishizawa, Kobayashi, Sakata, &

80   Kobayashi, 2015) and non-spatial working memory tasks (Furey, Pietrini, & Haxby, 2000;

81   Hasselmo, 2006; McGaughy, Koene, Eichenbaum, & Hasselmo, 2005).

82

83   To test the hypothesis, we constructed a biologically plausible model of the entorhinal-

84   hippocampal circuit consisting of MECIII, CA1 and MEC layer V (MECV) with ACh

85   projections from the medium septum and numerically simulated a DNMP task on a T

86   maze. We show that the cholinergic modulation of disinhibitory circuit in CA1 and a

87   calcium-dependent cation current in MEC is crucial for coordinating the encoding,

88   maintenance and retrieval modes of the MECIII-CA1-MECV circuit. The model

89   successfully reproduces theta phase preferences in various types of CA1 (Klausberger &

90   Somogyi, 2008) and MEC (Mizuseki, Sirota, Pastalkova, & Buzsáki, 2009) neurons.

91   Further, we demonstrate whether the inactivation of MECIII-to-CA1 input may impair

92   performance in DNMP tasks depends on the timing of inactivation, as was shown in

93   experiment (Yamamoto et al., 2014).

94

95   Our model also predicts that the same MECIII neurons encoding spatial information

96   retrieve this information later, which we confirm by analyzing experimental data of

97   single-cell and population-level activities. According to a widely accepted view, CA3-to-

98   CA1 input is responsible for retrieving spatial memory (Fernández-Ruiz et al., 2017; S. J.

99   Middleton & McHugh, 2016). However, a few studies suggested that MECIII-to-CA1

100 input is engaged in the recall of spatial memory (Suh et al., 2011; Yamamoto et al., 2014),

101 and our model supports the latter view.

102

103 **Results**

104 **Hippocampus-entorhinal cortex circuit model**

105 To clarify the circuit mechanisms to control flexibly spatial information in the

106 hippocampus and MEC, we built an inter-areal cortical network model (Figure 1A, see

107 Supplemental materials for details). The network comprises three main areas CA1, MEC

108 layer 3 (MECIII) and layer 5 (MECV), and includes additional areas CA3, MEC layer 2

109 (MECII) and the medial septum (MS) as external inputs. These external inputs oscillate

110 at theta frequency (10Hz) and entrain the main circuit to theta-frequency oscillation.

111 CA3 neurons encode the current location of model rat and transfer the location

112 information to CA1. All main areas have excitatory (E) and parvalbumin (PV)-positive

113 interneurons. In addition to these neurons, the model CA1 has somatostatin (SOM)-

114 positive oriens-lacunosum moleculare (OLM) and vasoactive intestinal polypeptide (VIP)

115 neurons. We built synaptic connections in our model based on anatomical observations

116 (Gonzalez-Sulser et al., 2014; Unal, Joshi, Viney, Kis, & Somogyi, 2015; Witter et al.,

117 2000). In addition, we assumed that E neurons in MECII project to PV neurons in MECIII,

118 as previously suggested (Mizuseki et al., 2009).

119

120 Acetylcholine (ACh) is known to modulate activity of VIP neurons (Albuquerque, Pereira,

121 Alkondon, & Rogers, 2009) and the conductance of calcium-sensitive non-specific cation

122 current (CAN) in MECV excitatory cells (Fransen, Alonso, & Hasselmo, 2002; Fransén,

123 Tahvildari, Egorov, Hasselmo, & Alonso, 2006). The concentration of ACh ([ACh]) is
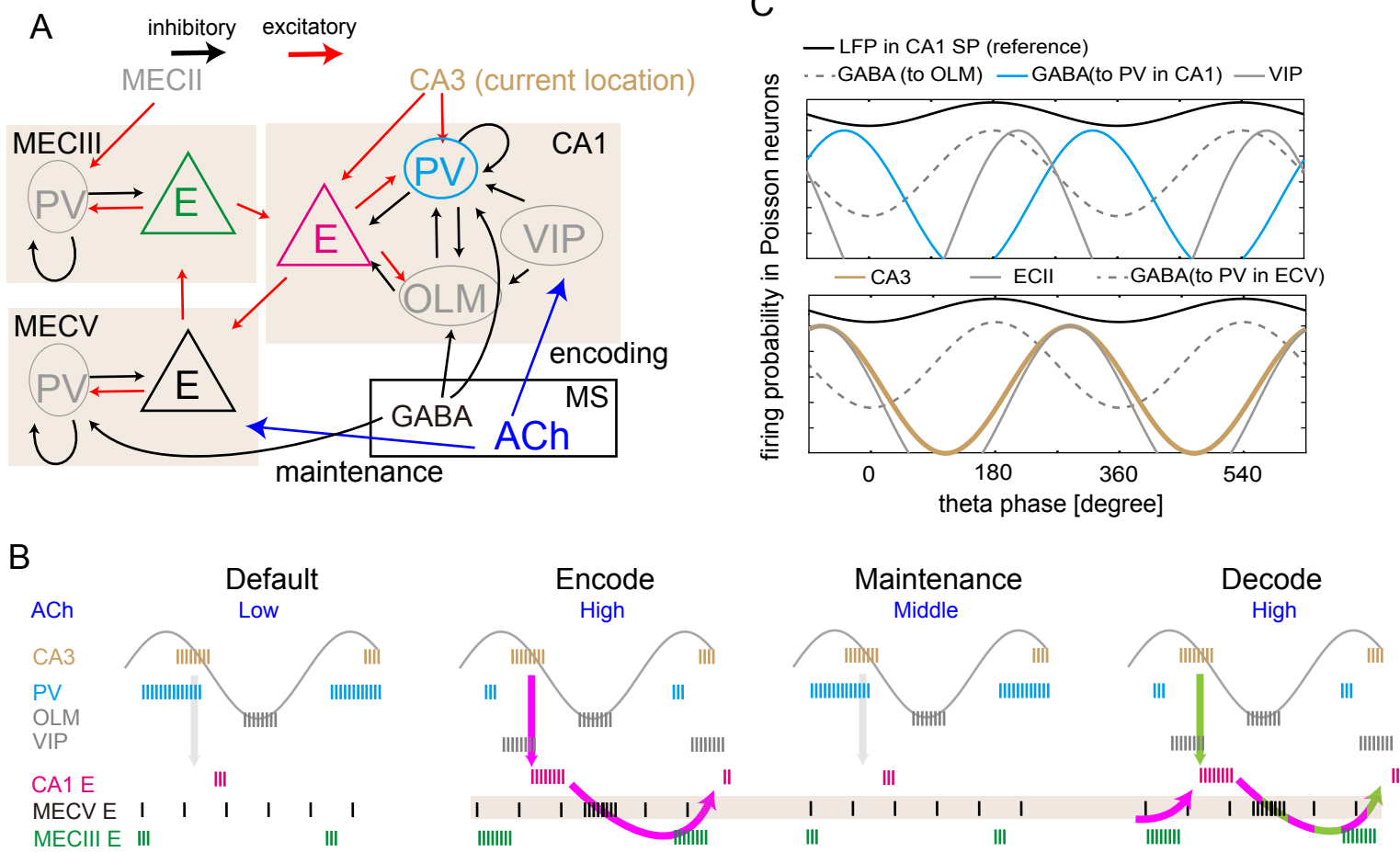
Figure 1

Figure 1. Entorhinal-hippocampal network model (A) Connectivity of the network model is shown. (B) Schematic image of the proposed mechanisms of spatial working memory. Vertical lines represent spikes of each neuron. Sinusoidal curve indicates theta oscillation in the CA1 stratum pyramidale (SP) layer. As described in C, this theta oscillation was used for a reference frame to measure the preferred phases of neuronal firing in our model. See the main text for details. (C) Theta-modulated firing probabilities of input neurons are shown during the sample-center run. The preferred firing phases were determined with respect to a reference theta oscillation (black) reported in the CA1 SP.

124   generally thought to change in a diffusive and tonic manner on slow timescales of

125   minutes or hours. However, recent studies have revealed that [ACh] undergoes rapid

126   phasic changes on sub-second and second timescales (Parikh et al., 2007; Teles-Grilo

127   Ruivo et al., 2017; H. Zhang, Lin, & Nicolelis, 2010). In this study, we assumed that [ACh]

128   varies in correlation with cognitive demands, i.e., [ACh] is high, slightly lowered and

129   again high during encoding, maintenance and recalling of working memory, respectively.

130   In contrast, the default concentration of Ach is low (Figure 1B). In reality, these

131   cholinergic modulations may be induced by MS (Newman, Gupta, Climer, Monaghan, &

132   Hasselmo, 2012; Okada et al., 2015; H. Zhang et al., 2010), but cholinergic neurons in

133   MS were not explicitly modeled in the present study. Under this model setting, we

134   tested the hypothesis that ACh controls information flow across the entorhinal-

135   hippocampal loop circuit in the different cognitive stages of a DNMP task. In particular,

136   we proposed and explored the possibility that [Ach] regulates the disinhibition of CA1 E

137   neurons and the calcium dynamics in MECV E neurons to enable the flexible processing

138   of spatial working memory.

139

140   Before showing the details of our network model, we schematically explain the

141   mechanisms of spatial working memory which we intend to propose in this study (Figure

142   1B). In the default stage (before encoding), [ACh] is low and activity of PV is high enough

143   to inhibit activity of CA1 E neurons and the flow of information on the current location

144   from CA3 to CA1 (shaded arrow in the panel of default stage). In the encoding stage,

145   [ACh] is set higher and consequently VIP neurons are activated, which in turn inhibits

146   CA1 PV neurons to enable the transfer of location information into CA1. Thus, the

147   location information is stored in the CA1-MECV-MECIII loop circuit (magenta arrows in

148   the panel of encode stage). Next, in the maintenance stage, [ACh] is at a middle level

149   and PV neuron activity is again high, blocking the re-entry of location information into

150   CA1. Despite this blockade, however, the spatial information is maintained by the

151   activation of calcium-dependent cation current in MECV E neurons without spike

152   generation. We assume that the current remains activated at the modest level of [ACh].

153   Finally, in the decoding stage, [ACh] is high again and information on the current location

6

154   is loaded from CA3 to CA1 (green arrow). It is noted that information on the previous

155   location maintained in MECV is also re-loaded from MECIII to CA1. Therefore, CA1

156   exhibits both current and previous position-encoding activities in the decoding stage.

157

158   The core circuits of the present network model consist of E, PV and OLM neurons , which

159   were modeled as Hodgkin-Huxley-type conductance-based neurons according to

160   previous models (S. Middleton et al., 2008; Rotstein, Oppermann, White, & Kopell, 2006;

161   Wang & Buzsáki, 1996; Wulff et al., 2009). VIP neurons were modeled as Poisson firing

162   neurons with a probability density of spikes and their outputs reflect the modulatory

163   effect of ACh. We described CA3 E neurons projecting to CA1, MECII E neurons

164   projecting to MECIII, and GABAergic neurons in MS projecting to CA1 and MECV as

165   external Poisson spike trains. As shown in Figure 1C, the firing probabilities of these

166   neurons were modulated at the theta-band frequency (10 Hz) to induce theta rhythmic

167   activities in the core circuits. The relative preferred theta phases of the external inputs

168   were chosen such that the preferred phases of various model neurons are consistent

169   with experimental observations (Klausberger & Somogyi, 2008; Mizuseki et al., 2009).

170   Furthermore, the relative phases between these inputs and theta oscillation in CA1 are

171   experimentally known, from which we can define the theta phase of the local field

172   potential (LFP) to be observed in the stratum pyramidale (SP) of CA1. This LFP oscillation

173   was used as a reference to measure the degree of agreement between the preferred

174   phases of model neurons and experimental observations. The preferred phases of

175   GABAergic neurons in MS were dependent on their target neuron types (ECV PV, CA1

176   PV and CA1 OLM). In experiment, GABAergic neurons projecting to OLM and those

177   projecting to PV in CA1 have different preferred phases (Borhegyi, 2004).

178

179   Given these settings of external theta-rhythmic sources, in a default stage the resultant

180   firing of all neurons in CA1, MECIII and MECV showed theta-rhythmic patterns and their

181   preferred phases are consistent with experimental observations (Figure S1): E and OLM

182   neurons in CA1 showed preferred phases around the troughs of theta oscillation,

183   whereas PV neurons around the peaks (Klausberger & Somogyi, 2008). In MECIII, E and
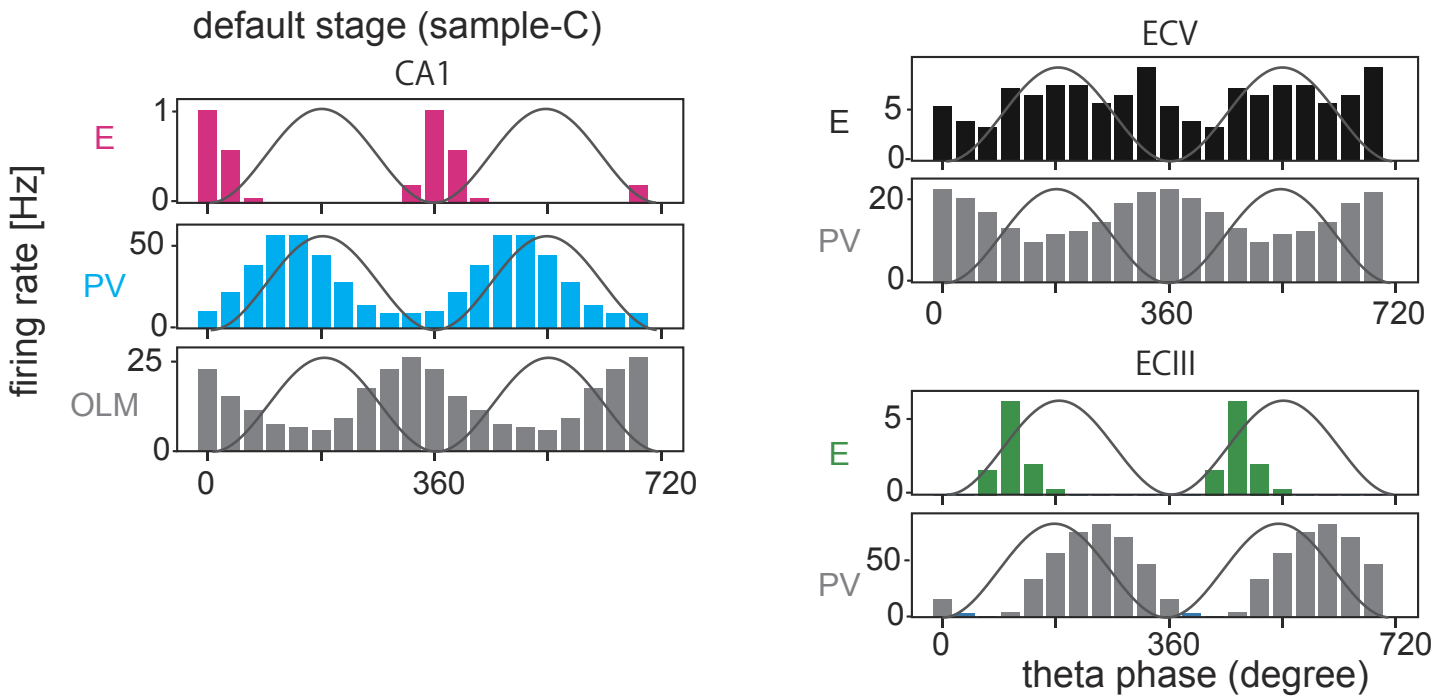
Figure S1

Figure S1 (related to Figure 1). Activity of various types of neuron during task. Preferred phases of various neuron types during the sample-C period. The firing rates were calculated by numerical simulations for excitatory and inhibitory neurons in the entorhinal-hippocampal circuit. The reference theta oscillation presumed in the SP layer of CA1 is also shown (solid lines).

184 PV neurons fired preferentially around the peaks and troughs of theta oscillation,

185 respectively (Mizuseki et al., 2009). In MECV, PV neurons preferred the troughs, but E

186 neurons did not show strong phase preferences (Mizuseki et al., 2009). Thus, the model

187 neurons show biologically plausible theta-phase locking activity.

188

189 **Encoding and recalling of spatial information in the circuit model**

190 The central question of this study is to clarify how spatial information is encoded,

191 maintained and recalled in the entorhinal-hippocampal circuits. Before studying this

192 problem, we, first, asked whether our model can replicate the task-related activities

193 reported in previous experiments. In particular, we considered a DNMP task on a T-maze

194 (Yamamoto et al., 2014). In this experiment, one arm of the T-maze was closed during a

195 sample run and the mouse was forced to choose another arm. After a delay period, the

196 mouse was set to a test run in which both arms were open and the mouse had to choose

197 the arm opposite to the one chosen in the preceding sample run (that is, if the mouse

198 chose the right arm in the sample run, it had to choose the left arm in the test run). For

199 a successful test run, the mouse had to remember the previously chosen arm. This task

200 requires at least two types of memory, namely, rule-based memory and spatial working

201 memory. The former memory is thought to be encoded in the prefrontal cortex

202 (Durstewitz, Vittoz, Floresco, & Seamans, 2010; Guise & Shapiro, 2017; Preston &

203 Eichenbaum, 2013). However, in this study we did not model the prefrontal circuits and

204 focused on the processing of spatial working memory in the entorhinal-hippocampal

205 circuits.

206

207 Figure 2A shows the organization of sample and test runs in our model together with

208 the connectivity patterns between the neural ensembles encoding different locations

209 on the maze. We monitored the activity of sample runs along the center arm (sample-

210 C) and left arm (sample-L), and that of test runs at the home position (delay) and center

211 arm (test-C) up to the junction (decision point) of the T-maze. For the sake of simplicity,

212 we implemented four subgroups L, R, C and H of place cells in CA3, each of which

213 encoded the current position of the model mouse on the left, right, center arms and at
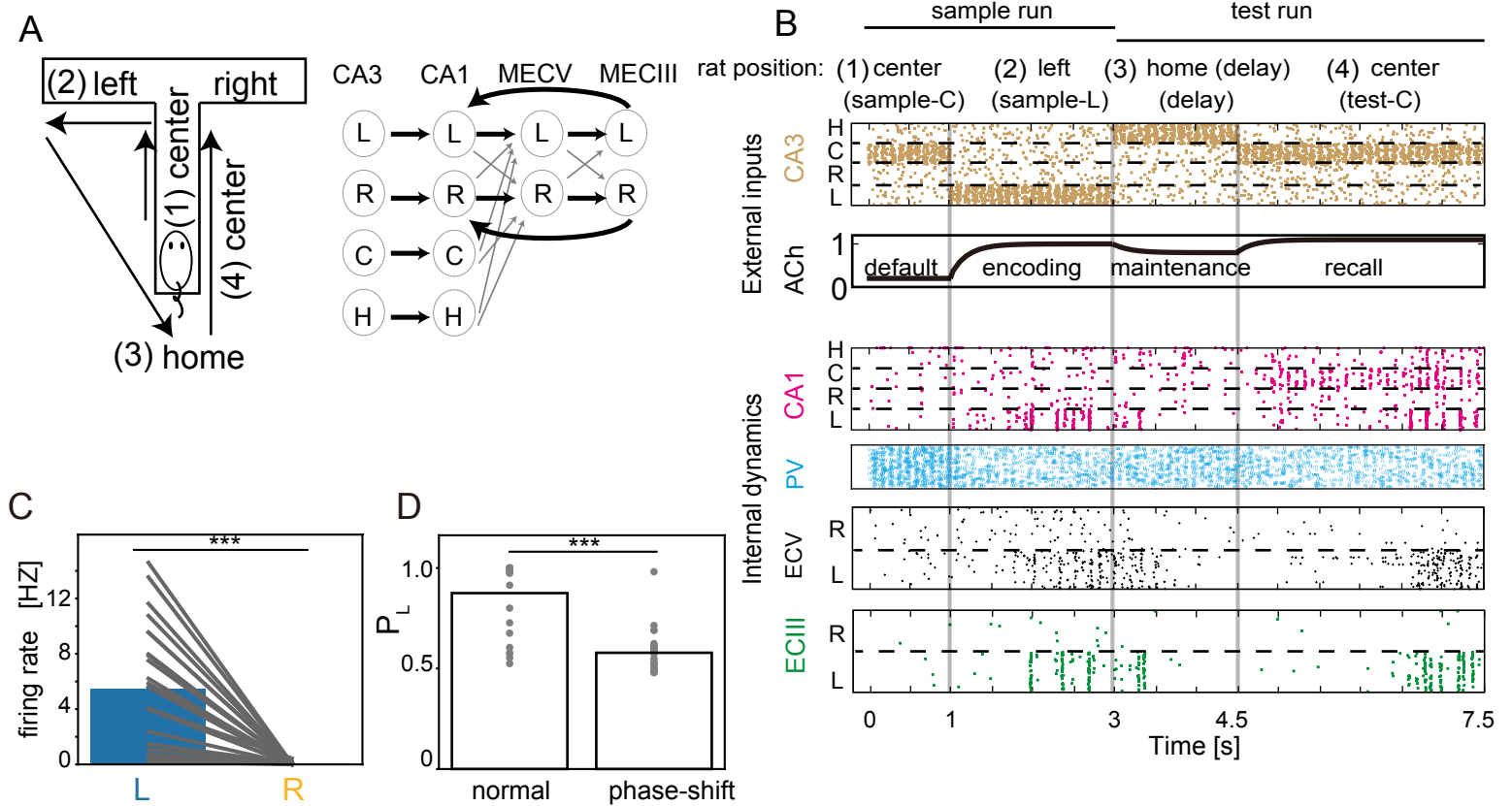
8

Figure 2

Figure 2. Performance of the model for a DNMP task (A) Left; Schematic illustrations of task periods during the sample and test trials of the DNMP T-maze task: (1) center in the sample trials (sample-C), (2) left in the sample trials (sample-L), (3) home (delay), (4) center in the test trials (test-C) periods. Right; Synaptic connectivity is shown between the neuron subgroups encoding the specific locations of the maze (left, right, center arms and home position). Connections (bold) are stronger within the loop circuit of MECV, MECIII and CA1 than other modest connections (solid). (B) Raster plots of E neurons in different cortical areas are shown together with the time evolution of ACh concentration. (C) The average firing rates of MECIII L and R subgroups were calculated for the test-C period in 25 runs of simulations (black lines, five different networks with five different initial conditions). Unless otherwise stated, average firing rates were evaluated in a similar fashion throughout this study. (D) Probability of left choice (P_L) and average of P_L was calculated in the normal and phase-shift conditions. Gray dots show P_L of different networks for different initial conditions. Chance level is 0.5.

214   the home position, respectively. For instance, neurons belonging to the subgroup L were

215   given a higher firing probability when the model mouse traveled across the left arm

216   (Figure 2B; also see "Neuron models" in Materials and methods). Accordingly, E neurons

217   in CA1 were also divided into four subgroups L, R, C, and H, each of which was strongly

218   projected to by the corresponding subgroup in CA3. In contrast, MECIII and MECV had

219   two subgroups denoted as L and R and these subgroups were assumed to form closed

220   loop circuits with the corresponding CA1 subgroups. In the present study, C and H

221   subgroups are not necessary in MEC and we omitted these parts for the sake of

222   simplicity. The other positions on the maze that are not shown in Figure 2A were not

223   modeled.

224

225   Below, without loss of generality, we consider the case that the mouse chooses the left

226   arm in every sample trial. Accordingly, we define task performance as the probability of

227   Left choice, P_L, which is estimated as $P_L = e^{-r_L}/(e^{-r_L} + e^{-r_R})$, where r_L and r_R are the

228   spike rates of the L and R subgroups, respectively, during the test-C period. Note that P_L

229   can be written as a function of $r_L - r_R$. The larger the difference in the spike rates, the

230   more robust the memory encoding.

231

232   In experiment, coherence between MECIII and CA1 increased in the high-gamma band

233   (60-120Hz) as the animal approached the junction point on the T-maze (Yamamoto et

234   al., 2014). The result indicates that high-gamma oscillation plays an active role in the

235   decision making, presumably in reading out stored locations from working memory.

236   However, the task performance of the animal was also highly correlated with theta-

237   phase-locked firing in MECIII. In addition, as shown later, our model successfully

238   performs working memory tasks without gamma oscillation. We speculate that high-

239   gamma oscillation nested in theta oscillation may either help the downstream areas

240   (responsible for the generation of behavioral outputs) to correctly read out the stored

241   locations from the entorhinal-hippocampal circuit or mediate top-down signals to shift

242   the status of the entorhinal-hippocampal circuit from the maintenance mode to the

243   readout mode. In this study, we focus on spatial information processing within CA1 and

244   MEC, and will not model any process arising outside of the entorhinal-hippocampal

245   circuit.

246

247   **Implications of preferred theta phases in coordinating activities in the CA1-MECV-**

248   **MECIII loop circuit**

249   In Figure 2B, we show activities of E neurons in CA3, CA1, MECV and MECIII together

250   with [ACh] during (1) sample-C, (2) sample-L, (3) home (delay) and (4) test-C runs.

251   Depending on the mouse's position, the corresponding subgroup was activated in CA3

252   according to the given firing probability. During the sample-L run, [ACh] was set to

253   increase, which disinhibited CA1 PV neurons and accordingly strongly activated the CA1-

254   MECV-MECIII loop circuit of the L subgroups to encode a choice memory in MECIII. Then,

255   in the delay period, [ACh] was set to decrease slightly, which strongly suppressed neural

256   activities in all L subgroups including the CA1 subgroup L. We note that a similar

257   suppression arose in experiment as if spatial memory had not been maintained during

258   delay periods (Yamamoto et al., 2014). During the test-C run, the CA1 subgroup C was

259   activated driven by the CA3 subgroup C. Importantly, as the model mouse approached

260   to the decision point, the subgroups L were gradually reactivated in the loop circuit to

261   retrieve the memory of the previous choice. This activation-suppression-reactivation

262   pattern is clearly seen in the firing rate of MECIII neurons. Average firing rates during

263   the test-C period were significantly different (p=3.071×10^{-6}, t test on two related

264   samples) between the subgroups L and R in MECIII (Figure 2C), implying that the network

265   model successfully recalled the stored spatial memory.

266

267   The successful encoding of memory required theta-phase-locking of neural firing along

268   the CA1-MECV-MECIII loop circuit. As mentioned previously, the theta phases of

269   external sources (i.e., CA3, MECII and MS) entrain neurons in these areas in theta-phase-

270   locked firing with the preferred phases that are consistent with experimental

271   observations. In the normal situation, MECIII PV neurons are activated by input from

272   MECII at the troughs of theta oscillation and consequently MECIII E neurons tend to fire

273   at the peaks. Then, CA1 E neurons are strongly activated in a non-linear manner(Bittner

274   et al., 2015; Takahashi & Magee, 2009) by near-coincident inputs from MECIII and CA3:

275   spikes from CA3 arriving at CA1 just after spikes from MECIII activate CA1 E neurons

276   much stronger than those from CA3 arriving at otherwise timing (see Materials and

277   methods).

278

279   The theta phases of inputs from the different sources were tuned such that they are

280   consistent with experimental observations (Figure 1C). Is this coordination of theta

281   phases necessary for successful working memory function? To examine this, we shifted

282   the preferred phases of MECII neurons by 180 degrees from the troughs to the peaks of

283   the reference theta oscillation of CA1 LFP (Figure S2A). Figure S2B shows the phase

284   preferences of CA3, CA1 E, CA1 PV, and MECIII E neurons after this change. MECIII PV

285   neurons dramatically reduced spikes at the descending phases of theta oscillation,

286   which shifted the firing of MECIII E neurons to the troughs of theta oscillation.

287   Consequently, the peak activities of MECIII and CA3 were separated by about one half

288   of theta cycle and did not coincidently innervate CA1. The timing deviation impaired the

289   encoding of spatial information into the loop circuit, as indicated by significantly

290   reduced rate differences between L and R subgroups (Figure S2C, p= 2.679×10^{-16}, t test

291   on two related samples), resulting in a degraded task performance (Figure 2D, p= 2.334

292    $\times 10^{-8}$, t test on two related samples). Thus, the specific coordination of the preferred

293   theta phases of MECIII and CA3 neurons is crucial for the working memory operation of

294   the entorhinal-hippocampal circuit.

295

296   **The role of disinhibition in regulating the activity of the CA1-MECV-MECIII loop circuit**

297   We show that the ACh-mediated disinhibitory mechanisms regulate cross-area

298   communications within the entorhinal-hippocampal circuit during different task periods.

299   We first analyzed how activity of CA1 E neurons is regulated by [ACh]. We consider the

300   default stage (i.e., 0 to 1 sec in Figure 2B) in which [ACh] is low (Figure 3A). In this stage,

301   output from VIP neurons is weakened and, consequently, PV and OLM neurons are

302   strongly activated around the peaks and the troughs of theta oscillation, respectively

303   (Figure 3B). Accordingly, CA1 E neurons rarely fire around the peaks and troughs (but
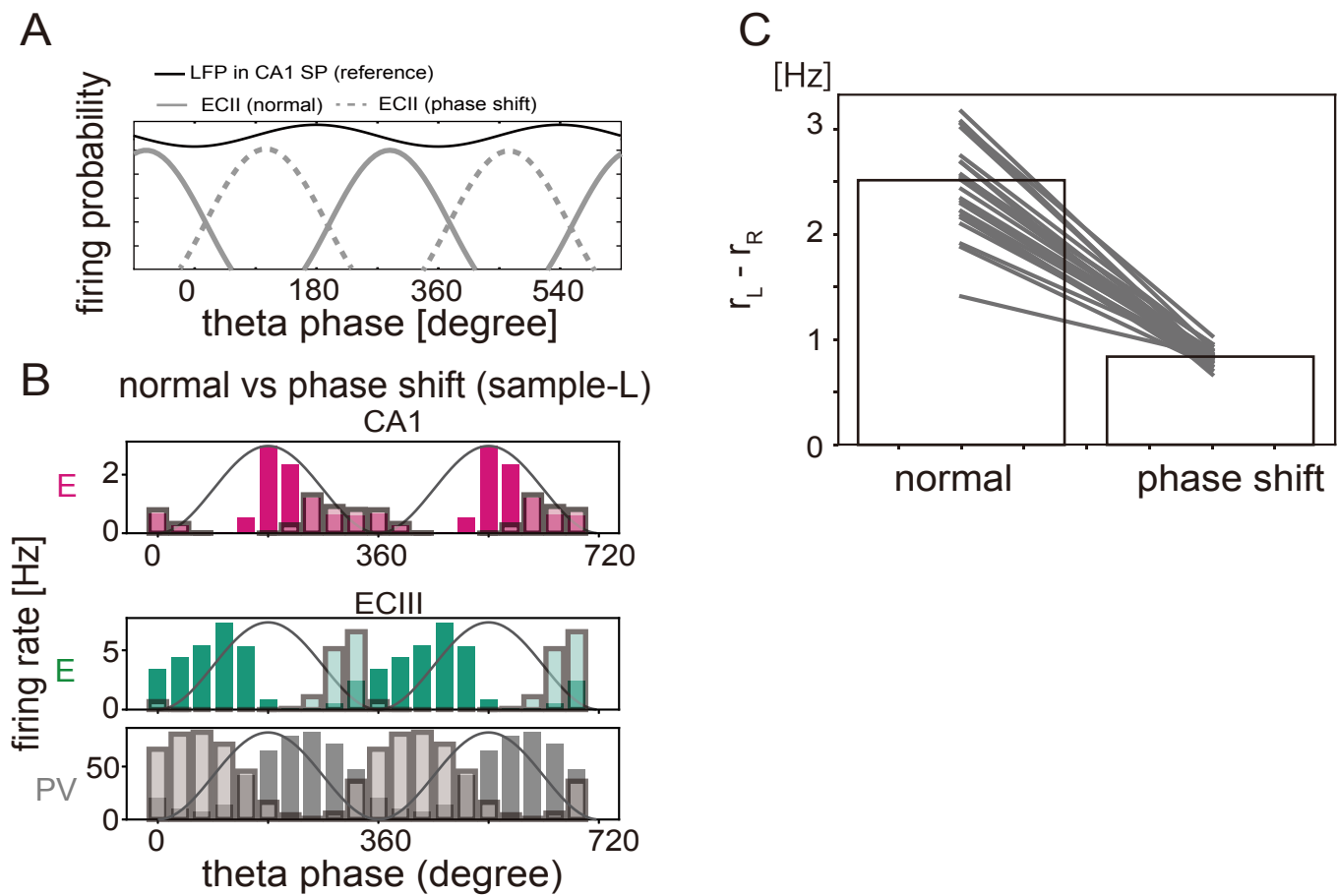
11

Figure S2

Figure S2 (related to Figure 2). (A) Theta-modulated firing probabilities of ECII neurons for the normal and preferred phase shift conditions are shown. (B) Modulations of spike counts by theta oscillation are shown for CA1 E, MECIII E and MECIII PV neurons during the sample-L period. Neuronal activities in the normal and preferred phase shift conditions of theta oscillation are shown with dark and light colors, respectively. (C) Differences in the firing rate between the L and R subgroups of CA1 E neurons were calculated during the sample-L period and compared between the normal and the phase shift conditions. Simulation results for the same initial conditions are connected with lines.
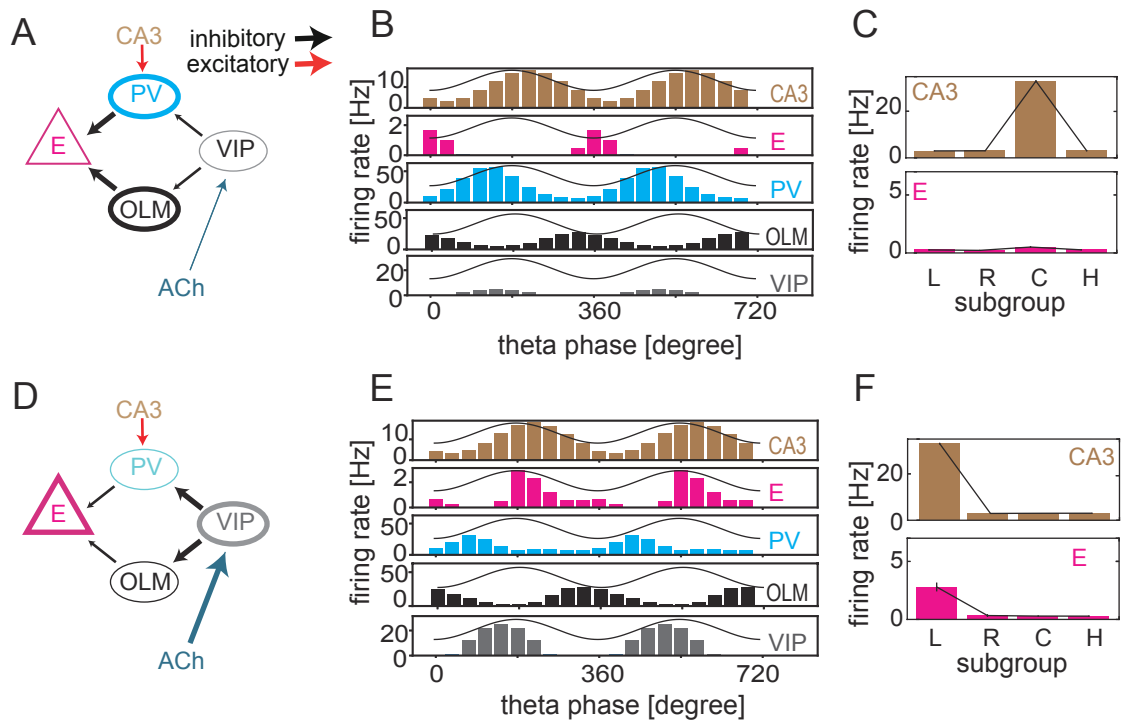
Figure 3

Figure 3. Gating of CA3-to-CA1 signaling by disinhibition mechanism. (A) The operation mode of disinhibitory circuit is schematically illustrated in low [ACh] states. (B) Theta phase preferences of spikes during the sample-C period are shown for CA1 neurons including all subgroups. Only for VIP neurons, the firing rate normalized by [ACh], which corresponds to output from VIP neurons to other inhibitory neurons (see the Materials and methods), is plotted. Solid curves show the reference theta oscillation. (C) Average firing rates of the L, R, C and H subgroups in CA3 and CA1 are shown during the sample-C period. Error bars indicate s.d. (D) The operation mode of disinhibitory circuit in high [ACh] states. (E, F) Similar to (B) and (C) during the sample-L period.

304   they can generate a small number of spikes driven by external noise after the troughs

305   of theta oscillation at which inputs from both PV and OLM are weakened: see Figure S1).

306   In contrast, during the epochs of high [ACh] (Figure 3D, the sample-L period: the test-C

307   period also corresponds to the high [ACh] epoch, but will be discussed later), CA1 E

308   neurons show strong activation immediately after the peaks of theta oscillation because

309   PV neurons are suppressed around the peak (Figure 3E). OLM neurons are also

310   suppressed, but their inhibitory effect on E-neuron firing around the peak is relatively

311   weak since the preferred phase of OLM neurons is the trough of theta (spikes around

312   the peak in Figure 3E are less than those in Figure 3B). Thus, [ACh] regulates the activity

313   of CA1 E neurons. Also, the cholinergic modulation advances the preferred phase of CA1

314   E neurons from the troughs to the peaks of theta oscillation. Later, we will examine the

315   model's prediction in experimental data.

316

317   Next, we asked if Information on the current position of the mouse can be selectively

318   transferred from CA3 to CA1 by [ACh]. Although, throughout the task, CA1 E neurons

319   constantly receive position information from CA3, a certain mechanism is required to

320   transfer CA3 position information to CA1 neurons selectively during encoding epoch (in

321   the sample-L period, see the CA1 L subgroups in Figure 2B). We found that ACh-induced

322   disinhibition provides this mechanism: at the sample-C period [ACh] is low and the

323   sensitivity of CA1 E neurons to CA3 input remains low, consequently the position

324   information is not transferred to CA1 (Figure 3C); at the sample-L period [ACh] is

325   increased and accordingly the sensitivity is also enhanced, resulting in an information

326   transfer (Figure 3F).

327

328   The disinhibition mechanism further explains why the blockade of MECIII-to-CA1

329   connections impaired task performance in experiment (Yamamoto et al., 2014). When

330   the model mouse is sampling left or right arm, the disinhibition mechanism enables the

331   activation of the corresponding subgroups in the CA1-ECV-ECIII loop: highly activated

332   CA1 neurons activate MECV E neurons, which in turn activate MECIII E neurons. MECIII-

333   to-CA1 projections further activate CA1 E neurons, thus completing a positive feedback

334 loop within the activated subgroups. However, the blockade of MECIII-to-CA1

335 connections reduces neural activity in CA1 and hence in MECIII, disabling the storage of

336 the current position.

337

338 To confirm the crucial roles of disinhibition (i.e., VIP-PV-E and VIP-OLM-E connections)

339 in the working memory task, we studied two cases. In the first case, PV neurons were

340 inactivated in CA1 during the entire trial period without changing the other conditions

341 (Figure S3A). Due to the lack of inhibition from PV neurons, CA1 E neurons were strongly

342 activated at any ACh concentration. In the encoding epoch, E neurons exhibited higher

343 activity in the L subgroup than in the R subgroup in both CA1 (Figure S3B) and ECIII

344 (Figure S3C, 1 to 3 sec). However, after this epoch E neurons immediately lost selectivity

345 to spatial information because they were too strongly activated in both subgroups.

346 During some intervals firing rate was higher in the L subgroup than in the R subgroup,

347 but it was opposite during other intervals (Figure S3C, after 3 sec). Thus, the spatial

348 information recalled randomly varied from trial to trial, and working memory

349 performance was unreliable (Figure S3D).

350

351 In the second case, the cholinergic modulation of PV neurons (but not that of OLM

352 neurons) was terminated during the entire trial period. In this case, PV neurons were

353 not inactivated even at high [ACh] (Figure S3E) and the encoding of spatial information

354 into CA1 was largely impaired (Figure S3F). Consequently, spatial information could not

355 be stably maintained in MECIII (Figure S3G) and probability of left choice, P_L, was

356 significantly decreased (Figure S3H, p=1.542×10^{-9}, t test on two related samples). Thus,

357 in both cases, spatial information in CA3 was not successfully transferred into the CA1-

358 MECV-MECIII loop circuit.

359

360 **Covert activation by calcium dynamics**

361 An unexpected experimental finding was that neural activities in MECIII were strongly

362 suppressed during delay periods (Yamamoto et al., 2014). This observation challenges

363 our hypothesis that either MECV or MECIII, or both, serve for working memory in the
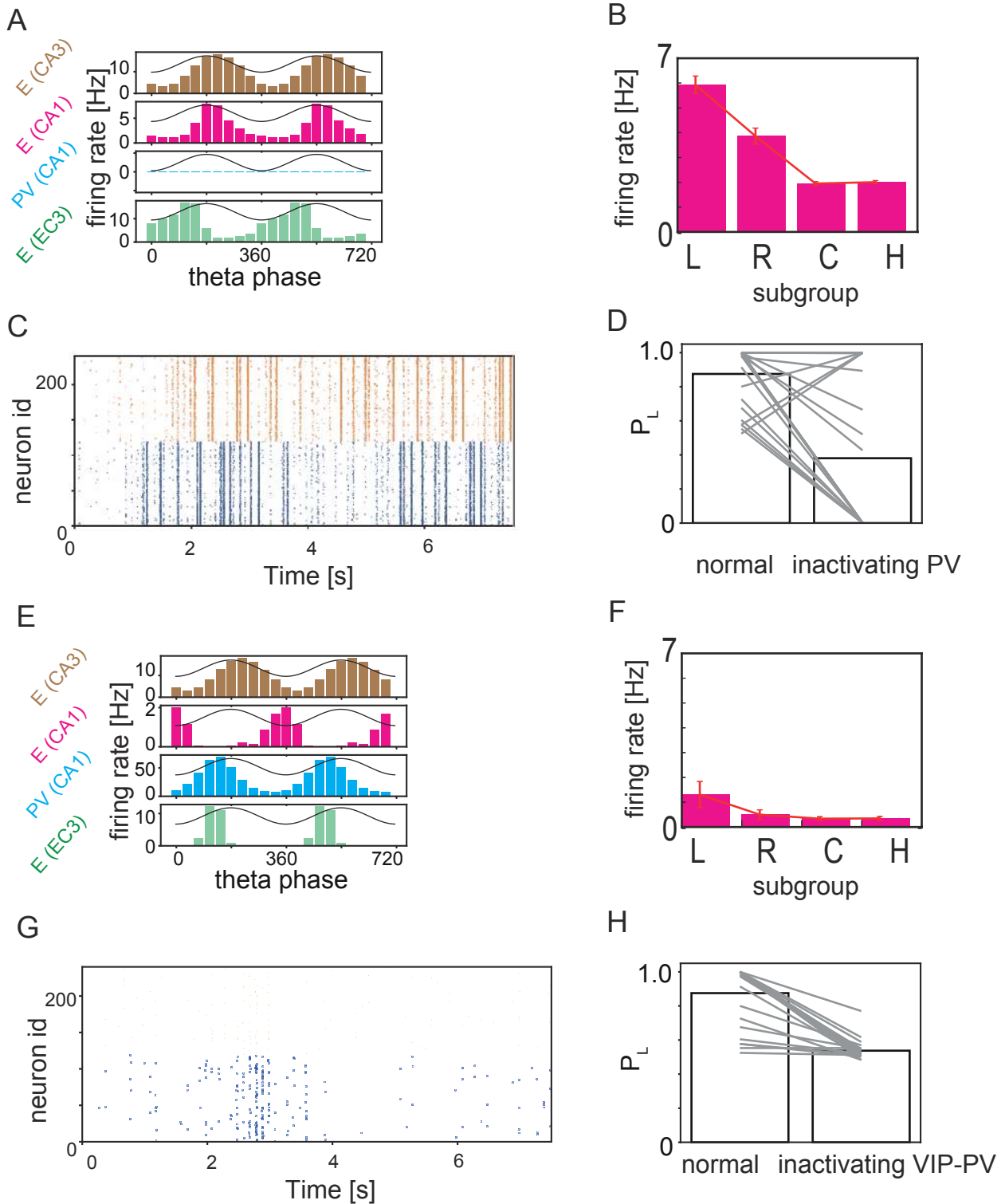
13

Figure S3

Figure S3 (related to Figure 3). Effect of inactivation of disinhibition mechanism. (A) Firing rates of CA1, CA3 and MECIII neurons during sample-L periods are shown. During the simulations, CA1 PV neurons were inactivated. Solid curves indicate the reference theta oscillation. (B) Average firing rates of CA1 E neurons in different subgroups are plotted during sample-L periods in the same inactivating condition. (C) Raster plots are shown for the L (blue) and R (orange) subgroups of MECIII E neurons. (D) Probability of left choice P_L is plotted in the normal and inactivating conditions. Lines connect two data points obtained from simulations of a normal network and its impaired version with the same initial conditions. (E, F, G, H) same as (A) to (D), but for the network models with disabled VIP-to-CA1 PV connections.

364   spatial decision making task, raising the question about how the entorhinal-

365   hippocampal circuit recalls the encoded spatial information after the delay periods. To

366   explore the underlying circuit mechanisms of memory recall, we implemented calcium-

367   sensitive non-specific cation current (CAN current in Materials and methods) in our

368   cortical neuron models.

369

370   The CAN current was originally proposed to explain persistent activity of single cortical

371   neurons in MECV (Fransen et al., 2002; Fransén et al., 2006), and a similar persistent

372   activity was later shown in the layer V of various cortical areas (Rahman & Berger, 2011).

373   The CAN current is activated in the presence of ACh with the intensity depending on the

374   activation rate of high conductance channels, r_H. The conductance r_H increases in time

375   when the calcium concentration $[Ca^{2+}]$ is beyond a critical value d_P and decreases when

376    $[Ca^{2+}]$ is below another critical value d_D. Because $d_D < d_P$, a hysteresis effect or bistability

377   appears for $d_D < [Ca^{2+}] < d_P$. Thus, once $[Ca^{2+}]$ exceeds d_P, the value of r_H remains high

378   until $[Ca^{2+}]$ again decreases below d_D (Figure 4A). Neurons with high r_H respond to input

379   more sensitively than those with low r_H and, thus, memory of previous high activity is

380   stored in r_H through calcium dynamics.

381

382   In the sample-L period, an increased activity of the CA1 subgroup L enhanced spike firing

383   of MECV E neurons in the subgroup L (Figure 4B). During the enhanced firing, $[Ca^{2+}]$ was

384   elevated in these neurons by calcium influx through the voltage-dependent calcium

385   channel. This increase of $[Ca^{2+}]$ occurred only in the MECV subgroup L but not in the

386   MECV subgroup R (Figure 4C). After the sample-L period, [ACh] was decreased and,

387   consequently, the CAN current was also decreased. Because lowering [ACh] decreased

388   the output of VIP neurons, that of PV neurons was increased and consequently that of

389   CA1 E neurons was suppressed. Thus, the changes in neural activity resulted in a

390   decreased firing rate of MECV E neurons. Nevertheless, the fraction of high conductance

391   state remained high in the subgroup L (but not in the subgroup R) of MECV E neurons
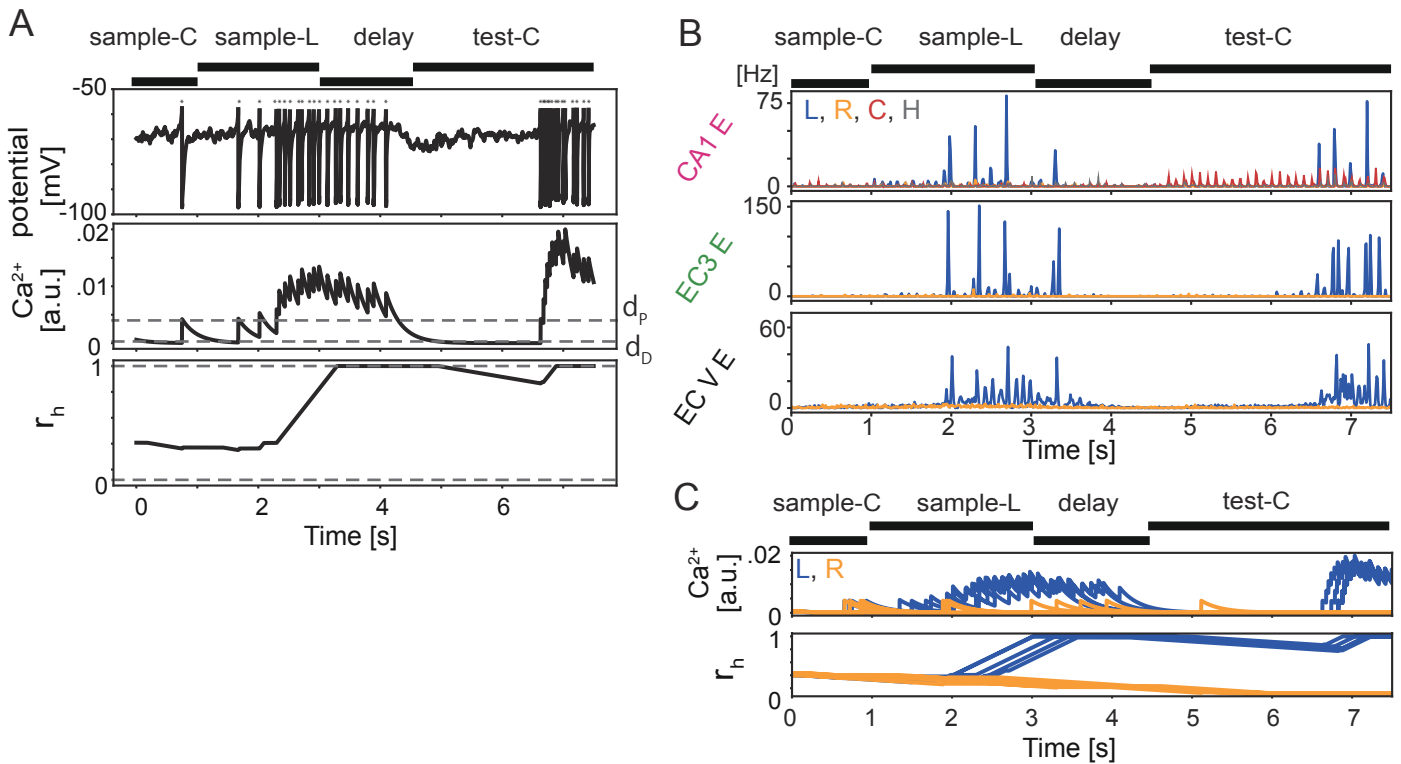
392   (Figure 4C).

393

Figure 4

Figure 4. Role of CAN current in memory encoding and maintenance. (A) Single trial evolution of the membrane potential (top), [Ca2+] (middle) and the ratio of high conductance state of CAN channels r_h (bottom) are plotted in an MECV excitatory neuron. Dots above the membrane potential represent spikes. Broken lines denote two threshold values, dP and dD, in the middle panel and the upper and lower critical values of the high conductance ratio in the bottom panel (See Materials and methods). (B) Firing rates are shown for E neurons in CA1, MECIII and MECV. Colors indicate different neuron subgroups. (C) Time evolution of [Ca2+] (top) and rh (bottom) are plotted for randomly-chosen five MECV E neurons belonging to L (blue) or R (orange) subgroup during the same trial as in B.

394 The CAN current plays a crucial role in the maintenance of working memory. To explain

395 this, we divided the test-C period into early and late periods: in the early period CA1

396 neurons were selectively activated in the subgroup C but not in the subgroup L (and

397 subgroup R); in the late period they were strongly activated in the subgroup L (Figure

398 4B). During the test-C period, [ACh] was again increased, so was the activity of CA1 E

399 neurons through the disinhibition mechanism. Although MECV neurons in both

400 subgroups L and R received synaptic input from the CA1 subgroup C, MECV neurons

401 were selectively activated in the subgroup L because the high conductance rate

402 remained high in these neurons. The activity of the MECV subgroup L neurons gradually

403 increased in the early test-C period, and eventually became sufficiently strong to

404 activate MECIII subgroup L neurons. Accordingly, the test-C period entered the late

405 period and the spatial information stored in MECV could be decoded by CA1 neurons.

406 The onset time of the late period depends on the realization of neural networks and

407 initial conditions. Thus, the covert activation of CAN current enables the retrieval of

408 persistent activity in the MECV subgroup L neurons for the decoding of spatial

409 information in the test-C period.

410

411 **Comparison of MECIII neural activity between the model and experiment**

412 We compared the responses of our model with those of the mouse entorhinal-

413 hippocampal circuit. For this comparison, we analyzed E neuron activity in MECIII after

414 dividing each of the sample-L, delay and test-C periods into early and late portions,

415 respectively. As in experiment (Yamamoto et al., 2014), we first quantified the intensity

416 of theta oscillation in these task periods by computing periodicity index (Materials and

417 methods). As shown in Figure 5A, this index was high during the late sample-L, early

418 delay, and late test-C periods, but it was low during delay period (i.e., late delay and

419 early test-C periods). Periodicity index exhibited similar task period-dependence in the

420 model and experiment (c.f. Figure 5C and Figure S5 in (Yamamoto et al., 2014)).

421

422 We next analyzed how the blockade of MECIII-to-CA1 projection affects the behavior of

423 our model in different task periods. In the experiment, this blockade significantly
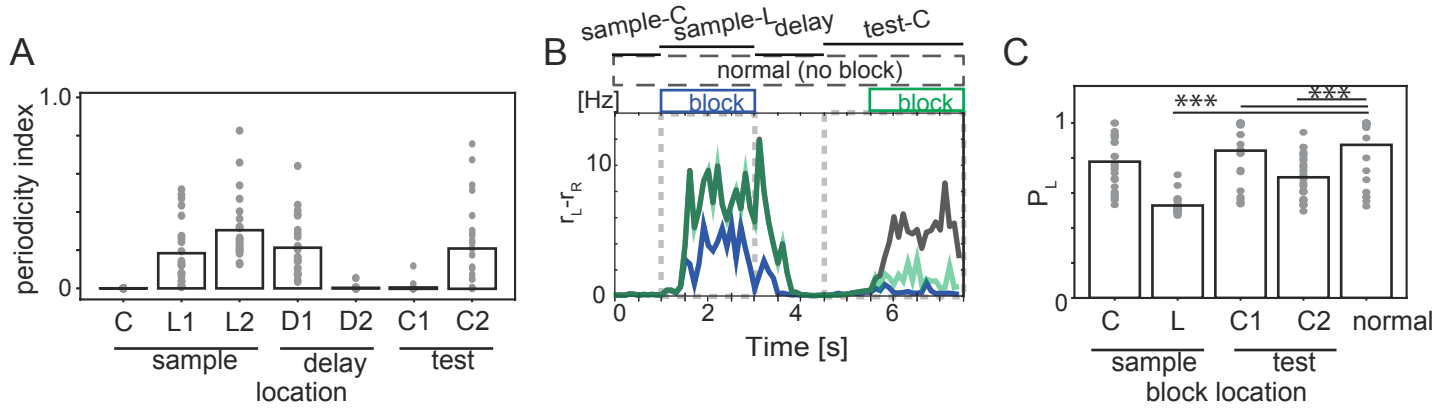
Figure 5

Figure 5. Blockade of MECIII-to-CA1 connections during sample-L and late test-C periods. (A) Periodicity index (Yamamoto et al., 2014) was calculated for the activity of MECIII E neurons (Materials and methods). The labels L, D, C refer to sample-L, delay, test-C periods, respectively, and the numbers 1 and 2 label the early and late portions, respectively, of these periods. (B) Average differences in firing rate between the L and R subgroups of MECIII E neurons were calculated under the blockade of MECIII-to-CA1 connections: normal condition (black); the blockade during sample-L periods (blue); the blockade during late test-C periods (green). In each condition, the differences were averaged over five networks and five initial states. By definition, green and black lines overlap with one another before the blockade. Boxes above the traces indicate the periods of blockade. (C) P_L were calculated for different periods of the blockade.

424   impaired working memory performance of the mouse. When MECIII-to-CA1 projection

425   was blocked during the encoding epoch (sample-L period), MECIII activity and the firing

426   rate difference between L and R subgroups were suppressed during both sample-L and

427   the subsequent late test-C periods (Figure 5B, blue), meaning that task performance was

428   impaired. When the blockade was during the recall epoch (late test-C, 5.5-7.5 s), the

429   inter-subgroup difference was reduced and task performance was also impaired (green

430   line in Figure 5B). In contrast, when the blockade was imposed during sample-C (3-4.5

431   s) or early test-C period (4.5-6 s), MECIII activity was not greatly affected (Figure S4).

432   Figure 5C summarizes the resultant task performance of the model. In three of the four

433   conditions (blockade in sample-C, early and late test-C), results were well consistent

434   with experimental observations (c.f., Figure 6F in (Yamamoto et al., 2014)). In addition,

435   our model predicts that the blockade in sample-L period significantly impairs working

436   memory performance ($p=3.175\times10^{-10}$), suggesting that the CA1-MECV-MECIII loop

437   circuit maintains neural activity in the MECIII and plays a pivotal role in the spatial

438   working memory task. This prediction should be experimentally validated.

439

440   **Experimental validation of period-dependent preferred theta phases**

441   Our model predicts that CA1 E neurons shift their preferred theta phases from the

442   troughs to the peaks when [ACh] is high (Figures 3B and 3E). In Figure 6A, we present

443   the phase preference of CA1 E neurons during sample-C, sample-L, delay, early test-

444   center (test-C1) and late test-center (test-C2) periods of the DNMP task. Their spikes

445   preferred the troughs of theta oscillation during sample-C periods but, owing to the

446   disinhibitory mechanism, the preferred phase was shifted to the peaks during sample-L

447   periods. When the model mouse returned to the home position (delay period), [ACh]

448   was decreased to reactivate PV neurons in CA1, which reduced the sensitivity of CA1 to

449   inputs from MECIII and CA3 and selectively suppressed spike generation at the peaks of

450   theta oscillation (but not at the troughs). In test-C1 periods, [ACh] was again increased

451   to allow the activation of CAN current (Figure 4C), which shifted the preferred phase to

452   the descending phase of theta oscillation. During test-C2 periods, our model predicts a

Figure S4

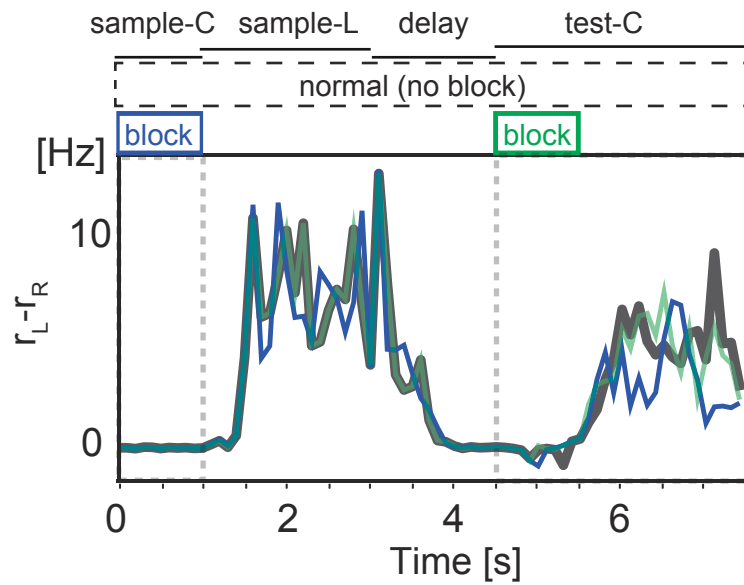Figure S4 (related to Figure 5). Blockade of MECIII-to-CA1 connections during sample-C and test-C periods. Connections from MECIII to CA1 were blocked during sample-C (blue) and early test-C (green) periods. Differences in firing rate between the L and R subgroups of MECIII E neurons are shown in the same manner as in Figure 5B. Similar evolutions are also shown in the normal condition (black).
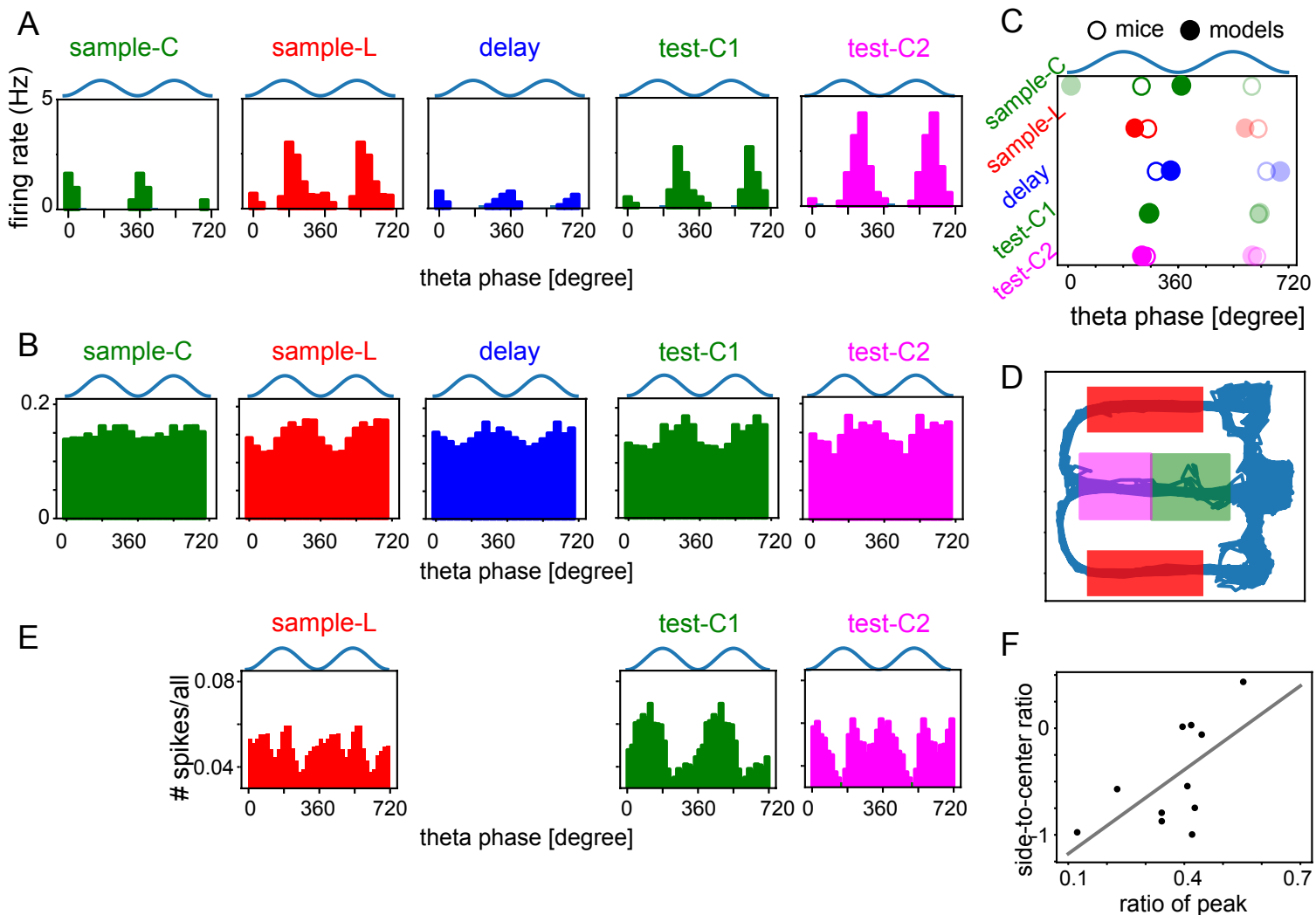
Figure 6

Figure 6. Preferred theta phases in model networks and rodents. (A) Phase preferences are shown for CA1 E neurons in model networks during given task periods (top). (B) Phase preference curves of CA1 neurons were calculated for data obtained in (Yamamoto et al., 2014). (C) Preferred theta phases of the models (filled circles) and mice (empty circles) were averaged over multiple theta cycles during given task periods. The same average phases are shown for two theta cycles (one in darker colors and one in light colors) for the clarity of the plots. (D) Schematic illustration of the figure-eight maze used in (Fernández-Ruiz et al., 2017; Mizuseki et al., 2013). Colored rectangles indicate early-center, late-center, and reward periods from which data were resampled. (E) Phase preference curves of CA1 excitatory neurons were calculated by using the data of (Mizuseki et al., 2013). For comparison, we divided the task periods of center arm and reward arm into early and late epochs. (F) Correlation between the ratios of spikes at the peaks and the side-to-center ratio is plotted.

453   progressive advance of preferred theta phase in CA1 due to an enhanced synaptic drive

454   by MECIII.

455

456   We confirmed these predictions in the data of a DNMP task in T-maze (Yamamoto et al.,

457   2014). Figure 6B shows the distributions of preferred phases of spikes in mouse CA1

458   during different task periods, i.e., sample-C, sample-L (corresponding to the reward arm),

459   delay, test-C1, and test-C2 periods (see Materials and methods). In mice, spikes were

460   generally not modulated by theta oscillation as strongly as in the model. In particular,

461   oscillatory modulations were weak in sample-C periods. Nonetheless, the preferred

462   theta phases in the various task periods are well consistent between mice and models.

463   The average preferred phase, which was computed as $\bar{\theta} = \arg\left(\Sigma_k \exp(i\theta_k)\right)$ with k

464   being the index of spikes for all neurons and i being imaginary unit, is delayed during

465   delay periods compared to other task periods in both mice and models (Figure 6C). In

466   contrast, our model predicts that the preferred phase is progressively advanced during

467   test-C2 (i.e., late test-center) period due to an increased synaptic drive by MECIII (Figure

468   4B).

469

470   Next, we asked whether preferred theta phase behaves similarly in an alternating figure-

471   eight task (Mizuseki, Sirota, Pastalkova, Diba, & Buzsaki, 2013). We were particularly

472   interested in examining the hypothesized role of cholinergic control of working memory

473   function. In the alternating figure-eight task, rats were trained to alternately change the

474   turn direction at a junction point of an eight-shape maze, meaning that the rats had to

475   remember the turn direction of the preceding run. This task is similar to the previous

476   DNMP task, but one difference is that sample and test trials are not clearly separated in

477   the alternating figure-eight task. Nevertheless, we may correlate the behavioral epochs

478   of the two tasks to each other. When rats traverse the center arm, they had to retrieve

479   memory of the preceding choice to prepare for the next choice. Therefore, traveling

480   along the center arm may correspond to test-C period in the DNMP task. Then, we can

481   define three distinct areas on the eight-shape maze (Figure 6D): early center, late center

482   and reward arms, which may correspond to test-C1, test-C2 and sample-L periods,

483   respectively. Below, we follow these rules.

484

485   Figure 6E shows the preferred phases of excitatory neurons in the deep layer of CA1. It

486   has been reported that for some unknown reason these neurons only exhibit phase

487   shifts in early trials (Fernández-Ruiz et al., 2017; Mizuseki et al., 2013). Therefore, we

488   only used data of initial ten trials in the following analyses. On the early center arm (test-

489   C1 period), neurons fired more frequently around the troughs of theta oscillation than

490   the peaks. However, on the late center arm (test-C2 period), neurons fired slightly more

491   often at the peaks, generating two peaks per theta cycle in the spike density distribution.

492   On the reward arm (sample-L period), neurons fired most frequently at the peaks, which

493   is consistent with the previous study(Fernández-Ruiz et al., 2017). These results seem to

494   be consistent with the model's prediction that the preferred firing phase of CA1 neurons

495   changes from the troughs to the peaks of theta oscillation during the epochs of high

496   [ACh]: in the alternating figure-eight task, high level of attention, or high [ACh], is likely

497   to be required on the reward arm (for encoding reward information) and the late center

498   arm (for recalling the previous choice).

499

500   Finally, we explored single-cell-level behavior in (Mizuseki et al., 2013) to provide further

501   support for our prediction: cells spiking on the side arms (cells in L or R subgroup in the

502   model) are likely to spike on the late center arm at the peaks of theta oscillation.

503   Therefore, we computed two ratios for 11 cells which showed high activation on the late

504   center arm (See Materials and methods for details): the number ratio of spikes

505   generated around the peaks (90° to 270°) to spikes generated on the late center arm;

506   the number ratio of spikes generated on the side arms to spikes generated on the late

507   center arm (side-to-center ratio). The values of the two ratios are significantly correlated

508   (Figure 6F: r=0.62 and p=0.042, t-test), suggesting that cells strongly activated on the

509   side arms are also highly likely to fire around the theta peaks. This result strongly

510   supports the prediction of our model.

511 **Task performance depends on acetylcholine concentrations in the model**

512 In our model, two ACh-regulated mechanisms, that is, disinhibitory circuit in CA1 and

513 CAN current in MECV excitatory cells, play crucial roles in encoding, maintenance and

514 recall epochs of working memory tasks. Therefore, we examined whether these core

515 mechanisms work robustly when [ACh] is changed. We changed the default levels of

516 [ACh] with other parameter values unchanged. Lowering the default [ACh], which

517 weakens disinhibition, during the encoding epoch (sample-L) disenabled the CA1 L and

518 R subgroups to exhibit large enough activity differences to encode spatial information

519 in the CA1-MECV-MECIII loop circuit (Figure 7A, blue). Task performance was severely

520 impaired, contrasting to intact performance at higher default [ACh] levels (Figure 7B,

521 left). Lower default [ACh] levels during delay period had almost no effects on task

522 performance (Figure 7B, center). Finally, lower default [ACh] levels during the recall

523 epoch (test-C2) eliminated the reactivation of the subgroup L (Figure 7A, green) and task

524 performance was severely impaired (Figure 7B, right), but performance remained intact

525 at higher [ACh] levels. These results show that default [ACh] levels should be sufficiently

526 high during the encoding and recall epochs, but fine tuning of [ACh] is unnecessary.

527

528 Next, we explored whether theta-phase-locked firing has anything to do with the

529 success of the working memory task. To this end, we compared the theta preference of

530 CA1 neurons during the test-C2 period between successful and failure trials in both

531 models and mice (Figure 7C). [ACh] was at the default levels. In both models and mice,

532 neurons preferentially fired around the peaks of theta oscillation in success trails, but

533 firing phases were somewhat delayed in failure trials.

534

535

536 **Discussion**

537

538 In this study, we developed a model comprising MECV, MECIII and CA1 to explore how

539 these local circuits process and communicate information with each other regulated by

540 ACh during DNMP tasks. In our model, changes in the ACh concentration control cortical
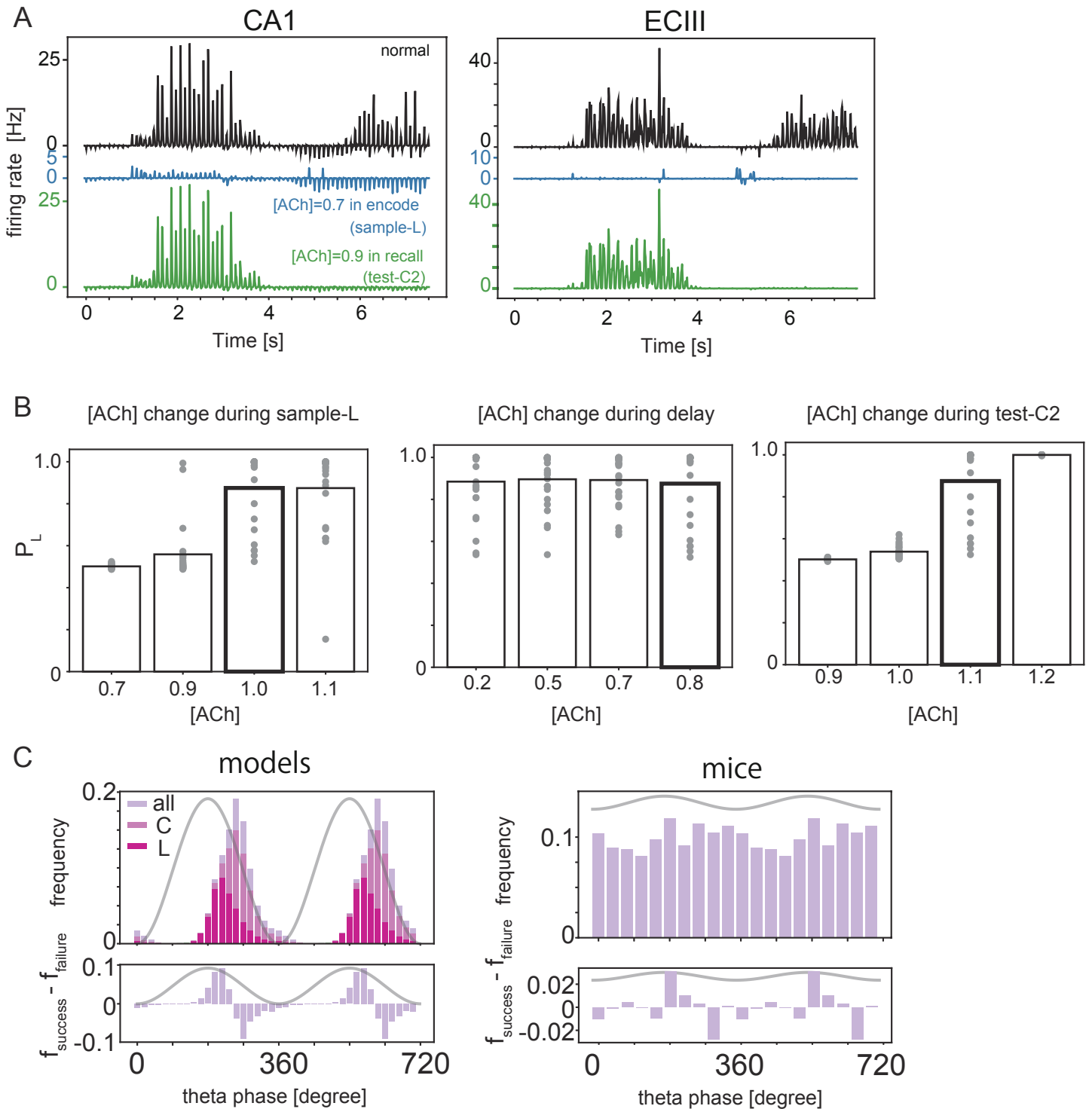
19

Figure 7

Figure 7. Cholinergic modulations in the network model. (A) In CA1 (left) and MECIII (right), differences in firing rate between the subgroups L and R were calculated at the normal (black) and reduced levels of [ACh] during encoding (sample-C, blue) and recall (test-C2, green) epochs. (B) Probability of left choice averaged over different networks and initial conditions are shown at different levels of [ACh] during sample-L (left), delay (center) and test-C2 (right) periods. Thick lines indicate results for the default [ACh] levels. (C) Frequency of spikes in CA1 excitatory neurons during test-C2 periods (top) are shown in the model (left) and mice (right). In the model, [ACh] was set to the normal level and spike counts are shown separately for the subgroups L and C. Only the total spike count is shown for mice. Bottom panels show the differences in firing rate between successful and failure trials.

541   disinhibitory systems and calcium-dependent cationic current to perform different

542   cognitive functions in DNMP tasks. With the ACh modulations, our model successfully

543   replicates the various features of neural activity observed in MECIII and CA1 (Yamamoto

544   et al., 2014). In particular, the model predicts that CA1 neurons change their preferred

545   theta phases depending on cognitive demands, which was also supported by

546   experimental data (Fernández-Ruiz et al., 2017; Mizuseki et al., 2013; Yamamoto et al.,

547   2014).

548

549   **Relevance of MEC-CA1 loop to spatial working memory tasks**

550   The hippocampal area CA1 is a central locus for spatial information processing, and

551   stores the concurrent position of the rodent (O'Keefe & Dostrovsky, 1971) as well as

552   retrospective and prospective representations of position information (Dragoi & Buzsáki,

553   2006; Ferbinteanu & Shapiro, 2003; Foster & Wilson, 2006; Gupta, van der Meer,

554   Touretzky, & Redish, 2010; Pastalkova, Itskov, Amarasingham, & Buzsaki, 2008; Zheng,

555   Bieri, Hsiao, & Colgin, 2016). Focusing on the CA1-MECV-MECIII loop circuit involved in

556   spatial working memory (van Strien, Cappaert, & Witter, 2009; Witter et al., 2000), we

557   demonstrated how the spatial information of the selected arm is encoded in CA1 during

558   a sample trial (Figure 3), maintained in MECV during delay period, and transferred to

559   MECIII and reloaded on CA1 for decision making (Figure 4). Several studies found that

560   connections from MECIII to CA1 are crucial for the success of spatial working memory

561   tasks (Suh et al., 2011; Yamamoto et al., 2014). Our model demonstrated this role of

562   MECIII-to-CA1 connections in spatial working memory, predicting their crucial

563   contribution to memory encoding by the entorhinal-hippocampal loop circuit. The

564   predicted operation of the loop circuit should be tested experimentally.

565

566   Sequence of spikes with theta phase precession, that is, "theta sequence" (Ferbinteanu

567   & Shapiro, 2003; S. J. Middleton & McHugh, 2016; Pfeiffer & Foster, 2013; Schlesiger et

568   al., 2015; Zheng et al., 2016), has been observed in the hippocampus and the MEC during

569   cognitive tasks requiring episodic memory. The blockade of MECIII-to-CA1 connections

570   causes modulation of theta activity in MECIII (Suh et al., 2011; Yamamoto et al., 2014).

571 Similarly, inactivation of the MEC disrupts the temporal organization of spikes and

572 impairs information maintenance (Robinson et al., 2017). These results imply that the

573 temporal coordination of theta-phase-locked neuronal firing along the CA1-MECV-

574 MECIII loop circuit is crucial for the success of spatial working memory tasks. We showed

575 an example case in which the disruption of this temporal coordination in MECIII led to a

576 significant increase of failure trials (Figure S2A, B).

577

578 Our model assumes that [ACh] changes in time during a working memory task and

579 predicts that these changes shift the preferred theta phase in CA1 E neurons: higher

580 [ACh] advances the preferred phase towards the peak of theta oscillation (Figure 6).

581 Specifically, the model predicts that phase advances occur during the encoding epoch in

582 sample trials (i.e., on the reward arm) and during the recall epoch in test trials (i.e., on

583 the center arm). We validated this prediction with the results of two experiments

584 (Fernández-Ruiz et al., 2017; Mizuseki et al., 2013; Yamamoto et al., 2014). Phase

585 advances in the encoding epoch have been known previously and can be accounted for

586 by temporal separation between CA3 input and MECIII input to CA1 (Colgin et al., 2009;

587 Cutsuridis, Cobb, & Graham, 2010; Hasselmo, Bodelón, & Wyble, 2002; Lasztóczi &

588 Klausberger, 2016; Milstein et al., 2015). Input from CA3 preferentially arrives at CA1 on

589 the descending phase of theta oscillation of LFP (Klausberger & Somogyi, 2008) whereas

590 input from MECIII arrives at the peaks of theta oscillation (Fernández-Ruiz et al., 2017;

591 Hasselmo et al., 2002; Mizuseki et al., 2009). Because MECIII input, which presumably

592 carries sensory information, seems to dominate CA3 input during encoding

593 (Hasselmo2002), CA1 neurons likely fire at the peaks rather than the troughs of theta

594 oscillation (Fernández-Ruiz et al., 2017).

595

596 Phase advances on the later central arm (i.e., in the recall epoch) represent a novel

597 finding of this study. CA1 neurons were previously shown to fire at the troughs of theta

598 oscillation during memory recall (Fernández-Ruiz et al., 2017), and this was consistent

599 with the view that CA3 input dominates MECIII input during this epoch. Challenging the

600 conventional view, our model predicts that CA1 neurons retrieve spatial memory from

21

601   the MECIII, hence firing at the peaks of theta oscillation. Possibly consistent with this

602   prediction, if we divide the center arm into early and late portions in (Mizuseki et al.,

603   2009), preferred theta phases show a second (and advanced) peak in the late portion of

604   recall epoch (Figure 6D). This peak was absent in the previous analysis (Fernández-Ruiz

605   et al., 2017) because the center arm was treated as a single entity. The consistency

606   between the model and experiment requires further clarification.

607

608   **Reflection of cognitive demands on the MEC-CA1 loop circuit through ACh**

609   ACh is involved with several cognitive functions such as sensory discrimination (Hangya

610   et al., 2015; Pinto et al., 2013), associative learning (Sabec et al., 2018), and spatial

611   (Croxson et al., 2011; Okada et al., 2015) and non-spatial working memory (Furey et al.,

612   2000; Hasselmo & Stern, 2006; McGaughy et al., 2005). In correlation with cognitive

613   states, ACh concentration changes to modulate activity of the specific types of neurons

614   (Muñoz, Tremblay, Levenstein, & Rudy, 2017; Womelsdorf et al., 2014) through

615   muscarinic and nicotinic receptors (Parikh et al., 2007; Teles-Grilo Ruivo et al., 2017; H.

616   Zhang et al., 2010). In associative learning, ACh was suggested to facilitate MECIII-to-

617   CA1 input during the encoding epoch and CA3-to-CA1 input during the decoding epoch

618   (Hasselmo, 2006). We propose a novel role and mechanism of ACh for the functions of

619   the entorhinal-hippocampal loop circuit according to the cognitive demands arising

620   during a spatial working memory task, namely, memory encoding, maintenance and

621   recall. Consistent with the proposal of our model (Figure 2B), it has recently been shown

622   in a DNMP task (Teles-Grilo Ruivo et al., 2017) that [ACh] is significantly higher on the

623   reward arm than in other positions in both sample and test trials, that on the center arm

624   [ACh] tends to be larger in test trials than in sample trials, and that [ACh] is low in delay

625   periods (c.f., Figure 7B).

626

627   We assumed that a change in cognitive demands is reflected in a phasic change in [ACh]

628   on the timescale of seconds. However, [ACh] is thought to change in a diffusive and tonic

629   manner on much slower timescales of minutes or hours. Importantly, recent studies

630   have revealed that [ACh] undergoes phasic changes at sub-second and second

22

631   timescales (Parikh et al., 2007; Teles-Grilo Ruivo et al., 2017; H. Zhang et al., 2010), and

632   such a phasic change in [ACh] is associated with reward or aversive signals (Hangya et

633   al., 2015). Further, task performance is correlated with slower tonic increases in [ACh]

634   during the task period (Parikh et al., 2007), but uncorrelated with phasic changes in

635   [ACh] in the reward arm (Teles-Grilo Ruivo et al., 2017). In our model, task performance

636   saturates above a certain level of [ACh] in the reward arm (Left panel in Figure 7B). Our

637   results suggest that the tonic level of [Ach] expresses an overall bias during each trial

638   and a phasic increase in [Ach] gives a more elaborate modulation reflecting a specific

639   cognitive demand.

640

641   **Dynamic processing across multiple areas**

642   Coherence in neural activity between different cortical areas varies with the cognitive

643   state of the brain (Benchenane et al., 2010; Fries, 2015). Furthermore, disruption of a

644   cortico-cortical interaction at different behavioral states can impair task performance

645   differently (Spellman et al., 2015; Yamamoto et al., 2014). These results imply that

646   information flows between cortical areas are differentially routed according to the

647   demand of the on-going cognitive process through the dynamical regulation of

648   corticocortical coherence. Theoretical studies have proposed several mechanisms of

649   information routing based on a balance control between excitatory and inhibitory

650   synaptic inputs (Vogels & Abbott, 2009), disinhibitory circuits (Yang et al., 2016),

651   spontaneous bursts (Palmigiano et al., 2017), and band-pass filtering by a feed-forward

652   inhibitory circuit (Akam & Kullmann, 2010). While these studies focused on the circuit

653   mechanisms of information routing, we addressed how such mechanisms are integrated

654   to perform a spatial working memory task through different cognitive demands

655   (Benchenane et al., 2010; Spellman et al., 2015; Yamamoto et al., 2014). We

656   demonstrated that cholinergic inputs coordinate the encoding and recall functions by

657   modulating the cortical disinhibitory circuit and Ca^{2+}-dependent cationic channels in

658   excitatory cells.

659

23

660   Accumulating evidence suggests that disinhibitory circuits play a crucial role in various

661   cognitive tasks such as fear conditioning (Letzkus et al., 2011; Pi et al., 2013) and sensory

662   discrimination (Hangya et al., 2015; Pinto et al., 2013). The dominant interneuron types

663   of the disinhibitory circuits are VIP, SOM and PV inhibitory neurons (Donato, Rompani,

664   & Caroni, 2013; Francavilla et al., 2018; Kamigaki & Dan, 2017; S. Zhang et al., 2014).

665   Among these neurons, VIP neurons express muscarinic receptors and are depolarized

666   by cholinergic input (Bell, Bell, & McQuiston, 2014) and are thought to project more

667   strongly to SOM neurons than to PV neurons in cortical areas (Kamigaki & Dan, 2017; S.

668   Zhang et al., 2014). However, some studies suggest stronger cholinergic modulations of

669   PV neurons in the hippocampus (Donato et al., 2013; Francavilla et al., 2018). As

670   explained below, the cholinergic modulation of OLM neurons also does not strongly

671   influence the firing of CA1 E neurons. Therefore, in this study we mainly analyzed the

672   effect of PV neurons on neural circuit functions. In line with our model's prediction

673   (Figure S3), optogenetic inhibition of PV neurons impairs performance in spatial working

674   memory (A. J. Murray et al., 2011).

675

676   PV neurons which preferentially fire in the descending phase of theta oscillation

677   (Klausberger & Somogyi, 2008) to weaken the effect of CA3-to-CA1 input. In contrast,

678   SOM (OLM in CA1) neurons preferably spike at the troughs of theta oscillation

679   (Klausberger & Somogyi, 2008; Royer et al., 2012) much earlier than the CA3 input. In

680   our model, excitatory MECIII input innervates CA1 preferentially at the theta peaks but

681   rarely at the theta troughs. Therefore, the ACh-induced suppression of OLM neurons

682   does not also enhance the effect of MECIII input on excitatory neuron firing in CA1,

683   making OLM neurons less effective than PV neurons in modulating the CA1 activity. In

684   rats, however, the actual spikes delivered by the MECIII are distributed broadly over a

685   theta cycle (Mizuseki et al., 2009), implying that the suppression of PV and SOM neurons

686   can induce a complex modulatory effect in CA1 pyramidal neurons. Our model predicts

687   that the inactivation of PV or VIP neurons (in this case both PV and SOM are released

688   from the inhibition by VIP neurons) impairs task performance in different ways (Figure

689   S3). This prediction needs to be confirmed by experiments.

24

690

Covert memory state for maintenance of information

Recent studies showed that dynamically evolving neuronal activity can maintain information during a delay period in working memory tasks (J. D. Murray et al., 2017; Stokes, 2015; Wolff, Jochim, Akyürek, & Stokes, 2017). In the DNMP task we studied (Yamamoto et al., 2014), theta phase-locked firing of MECIII neurons was correlated with the success of the task. Nevertheless, this neuronal activity temporarily vanished during a delay period, implying that a non-spiking activity maintains information on the previous choice. We hypothesized that the conductance of a specific ionic channel, i.e., calcium-dependent cationic current, remains in an elevated state to preserve spatial information during delay period. This elevated state is not accompanied by neuronal firing, hence is consistent with experimental observations. This mechanism was originally proposed to account for persistent activity of isolated single neurons (Fransen et al., 2002; Fransén et al., 2006) and suggested to be engaged in temporal association memory (Kitamura et al., 2014). Our model demonstrates that the same mechanism can generate a covert memory state necessary in spatial working memory. This and other mechanisms of covert memory state, for instance, short-term synaptic plasticity (Mongillo, Barak, & Tsodyks, 2008), are not mutually exclusive. However, our mechanism has an important advantage that working memory maintenance is turned on and off by cholinergic modulation depending on the cognitive demand. Thus, our results suggest that neuromodulators are crucial for the flexible control of memory processing by the brain.

Limitation of the model

First, while our model indicates that a success in spatial working memory tasks requires the adequate preferred theta phases of MEC and hippocampal neurons, experimental results suggest an active role of high-gamma oscillation (60-120 Hz) in working memory tasks (Yamamoto et al., 2014). In our model, theta-phase-locked neuronal firing is sufficient for successful information transfers along the MECIII-CA1-MECV loop circuit and gamma oscillation was not modeled. We speculate that gamma oscillation may

25

720   significantly facilitate the decoding of information stored in the entorhinal-hippocampal

721   circuit from its outside. The role of gamma oscillation in spatial working memory needs

722   to be further explored.

723

724   Secondly, we did not model any mechanism to translate the decoded information into

725   a correct choice behavior under a given rule of decision making (e.g., the alternative of

726   left or right turn). The mPFC is projected to by CA1 and projects back to it via reuniens

727   (Dolleman-Van Der Weel & Witter, 1996; Ito, Zhang, Witter, Moser, & Moser, 2015), and

728   is engaged in spatial working memory (Bolkan et al., 2017; Jones & Wilson, 2005;

729   Spellman et al., 2015). Furthermore, some mPFC neurons exhibit rule-related activities.

730   However, the delay-period activity of mPFC neurons is specific to neither previous nor

731   present location in a DNMP task (Bolkan2017) and the rule-related activities are not

732   location-specific (Durstewitz et al., 2010; Guise & Shapiro, 2017; Preston & Eichenbaum,

733   2013). Where and how decision rules are processed and how spatial working memory

734   and rule-related activities are integrated are open to future studies.

735

736 **Materials and methods**

737

738 **Neuron models**

739 Our model has two classes of neurons: i) Poisson neurons; ii) Hodgkin-Huxley type (HH)

740 neurons.

741 i) Poisson neurons

742 There are four types of theta-oscillating neurons (excitatory neurons in CA3 and MECII,

743 VIP neurons in CA1 and GABAergic neurons in MS) and noise neurons. Other types of

744 neurons, that is, excitatory (E) neurons, fast spiking (PV) neurons and OLM neurons in

745 CA1, E and PV neurons in MECIII and E and PV neurons in MECV, are modeled as HH

746 neurons. 40 excitatory and 40 inhibitory noise neurons project to all HH neurons. Firing

747 rates of noise neurons are different depending on the cortical areas modeled: 35 [Hz] in

748 CA1 and in MECIII and 30 [Hz] in MECV.

749 For theta-oscillating Poisson neurons, we described the theta-oscillating (10Hz)

750 probability of spiking per unit time $P_x(t_1 < t < t_1 + \Delta t)$ (x=E in CA3 and MECII, VIP in

751 CA1, GABA in MS) as

752 $$P_x(t_1 < t < t_1 + \Delta t) = (\Theta(A_x \left(sin \left(2\pi \left(\frac{t}{T} - \theta_x \right) \right) + B_x \right)) + C_x)\Delta t,$$

753 where $\Theta(s) = s$ when $s>0$ or otherwise 0. $T = 100$ ms and $\Delta t = 0.02$ ms is the step size

754 of our numerical simulation. A_x and B_x are the amplitude and preferred phase of

755 oscillating firing rate, respectively, and θ_x is the preferred phase of theta oscillation for

756 the neuron type x, whereas C_x is the amplitude of background noise for inactive

757 subgroups outside of their place fields. We set the preferred phases based on previous

758 experimental studies (Borhegyi, 2004; Klausberger & Somogyi, 2008; Mizuseki et al.,

759 2009) as follows:

760

761 x = E in CA3:

762 CA3 neurons in the model are divided into four groups according to their spatial

763 preferences (Figure 2 and Circuit structure in Materials and methods). Their firing

764 patterns are changed depending on the present location of the model rat. When the

765 model rat is in Center ($0 < t < 1000$ ms, sample-C and $4500 \leq t < 7500$ ms, test-C),

766 sample-Left ($1000 \leq t < 3000$ ms) and Home ($3000 \leq t < 4500$ms) positions, Center,

767 Left, and Home subgroups are activated, respectively.

768 $A_x = 30$ [Hz], $B_x = 1, C_x = 0$ [Hz], $\theta_x = -0.2$

769 for neurons in an active subgroup, and

770 $$A_x = 0 \text{ [Hz]}, C_x = 3 \text{ [Hz]}$$

771 for neurons in inactive subgroups.

772

773 x = ECII:

27

774 During the entire trial period, we set the parameters as

$$A_x = 5 \text{ [Hz]}, B_x = 0.6, C_x = 0 \text{ [Hz]}, \theta_x = -0.2$$

776

777 *x* = GABAergic in MS:

778 Three groups exist in the model, those projecting to PV in CA1, to OLM in CA1 and to PV

779 in MECV. The preferred theta phase of MECV PV-projecting GABAergic neurons is the

780 same as that of CA1 OLM-projecting GABAergic neurons,

781 $A_x = 5[Hz], B_x = 0.8, C_x = 0[Hz], \theta_x = -0.1,$

782 whereas the preferred phases of CA1 PV-projecting neurons are different from the

783 above ones (Borhegyi, 2004) and given by

784 $A_x = 5[Hz], B_x = 2.0, C_x = 0[Hz], \theta_x = -0.5.$

785

786 *x*=VIP:

787 During the entire trial period, we set the parameters as

$$A_x = 20[Hz], B_x = 0.3, C_x = 0[Hz], \theta_x = -0.4.$$

789

790 Finally, we set a reference theta oscillation in CA1 SP as

$$A_x = 1, \theta_x = 0.5, B_x = 0, C_x = 0,$$

792 which is a virtual oscillatory component used only for determining the relative oscillation

793 phases of other brain regions to theta oscillation in CA1 SP, but not for numerically

794 simulating the network model.

795

796 ii) HH neurons

797 In our model, there are seven types of neurons; E, PV and OLM in CA1, and E and PV in

798 MECV and MECIII. PV neurons are modeled identically in all areas (Wang & Buzsáki,

799 1996). In the following equations, I_i is synaptic input from other neurons as described

800 in Circuit structure in Materials and methods. Dynamics of each type of neurons is

801 described below.

802

803 a) Excitatory neurons in CA1

804 We modeled excitatory neurons in CA1 based on (Wulff et al., 2009). We additionally

805 included an afterhyperpolarization (AHP) and h currents in the model for generating a

806 weak subthreshold oscillation of the membrane potentials through interplay between

807 AHP (S. Middleton et al., 2008) and h current (Rotstein et al., 2006).

808 $V_{Na} = 50[mV], V_K = -100.0[mV], V_{AHP} = -100.0[mV], V_h = -20.0[mV], V_L$

809 $= -67.0[mV]$

810 $g_{Na} = 100.0[mS/cm^2], g_K = 80.0[mS/cm^2], g_{AHP} = 0.2[mS/cm^2], g_h$

811 $= 0.1[mS/cm^2], g_L = 0.1[mS/cm^2]$

812 $C = 1\,[\mu S/cm^2], I_{cnst} = -0.1\,[\mu A/cm^2]$

813 $$C\frac{dV_i}{dt} = g_{Na}m_\infty(V)^3 h(V_{Na} - V_i) + g_K n^4(V_K - V_i) + g_{AHP}w(V_{AHP} - V_i)$$

814 $$+ g_h(0.65hf + 0.35hs)(V_h - V_i) + g_L(V_L - V_i) + I_i + I_{const}$$

815 The channel variable h is determined as

816 $h = \max(1 - 1.25n, 0)$.

817 Other channel variables evolve according to

818 $\frac{dx}{dt} = \frac{x_\infty(V) - x}{\tau_x(V)}$,

819 where x = m, n, w, hf and hs. Among these variables, m and n are determined by

820

821 $x_\infty(V) = \frac{\alpha_x(V)}{\alpha_x(V) + \beta_x(V)}$,

822 $\tau_x(V) = 1/(\alpha_x(V) + \beta_x(V))$,

823 where x stands for either m or n, and

824 $\alpha_m(V) = -0.32(V + 54)/(\exp(-0.25 * (V + 54)) - 1$,.

825 $\beta_m(V) = 0.28(V + 27)/(\exp(0.2 * (V + 27)) - 1)$,

826 $\alpha_n(V) = -0.032(V + 52)/(\exp(-0.2 * (V + 52)) - 1)$,

827 $\beta_n(V) = 0.5\exp(-0.025(V + 57))$.

828 Other variables are determined by

829 $$w_\infty(V) = \frac{1}{\exp(-0.1(V + 41)) + 1}$$

830 $$\tau_w(V) = \frac{500}{3.3\exp(0.05(V + 41)) + \exp(-0.05(V + 41))}$$

831 $$hf_\infty(V) = 1/(1 + \exp\left(\frac{V + 79.2}{9.78}\right))$$

832 $$\tau_{hf}(V) = \frac{0.51}{\exp((V - 1.7)/10) + \exp(-(V + 340)/52)} + 1$$

833 $hs_\infty(V) = 1/\left(1 + \exp\left(\frac{V + 2.83}{15.9}\right)\right)^{58}$

834 $\tau_{hs}(V) = \frac{5.6}{\exp\left(\frac{V - 1.7}{14}\right) + \exp\left(\frac{-(V + 260)}{43}\right)} + 1$.

835

836 b) PV in CA1, MECIII, MECV

837 We modeled PV neurons in CA1 as well as those in MECIII and MECV as described in

838 (Wang & Buzsáki, 1996).

839 $$V_{Na} = 55[mV], V_K = -90.0[mV], V_L = -65.0[mV]$$

840 $$g_{Na} = 35.0[mS/cm^2], g_K = 9.0[mS/cm^2], g_L = 0.1[mS/cm^2]$$

841 $$C = 1[\mu F/cm^2]$$

842 $$C\frac{dV_i}{dt} = g_{Na}m_\infty(V)^3 h(V_{Na} - V_i) + g_K n^4(V_K - V_i) + g_L(V_L - V_i) + I_i$$

843
$$\frac{dx}{dt} = \frac{x_\infty(V) - x}{\tau_x(V)}$$

844
$$x_\infty(V) = \frac{\alpha_x(V)}{\alpha_x(V) + \beta_x(V)}$$

845     $\tau_x(V) = 1/(\alpha_x(V) + \beta_x(V))$,

846   where the index $x = n$, h and m.

847
$$\alpha_m(V) = 0.1(V + 35)/(1 - \exp(-0.1(V + 35)))$$

848
$$\beta_m(V) = 4\exp\left(-\frac{V + 57}{40}\right)$$

849
$$\alpha_n(V) = 0.01(V + 34)/(1 - \exp(-(V + 34)))$$

850
$$\beta_n(V) = 0.125\exp\left(-(V + 44)/80\right)$$

851
$$\alpha_h(V) = 0.07\exp\left(-(V + 58)/20\right)$$

852
$$\beta_h(V) = 1/(\exp(-0.1(V + 28)) + 1)$$

853

854   c)   OLM in CA1:

855   We modeled OLM neurons as described in (Wulff et al., 2009).

856     $V_{Na} = 60[mV], V_K = -100.0[mV], V_L = -70.0[mV], V_A = -90.0[mV], V_h$

857     $= -32.0[mV]$

858     $g_{Na} = 40.0[mS/cm^2], g_K = 23.0[mS/cm^2], g_A = 16.0[mS/cm^2], g_h$

859     $= 6.0[mS/cm^2], g_L = 0.05[mS/cm^2]$

860     $C = 1.3[\mu S/cm^2], I_{cnst} = 0.2[\mu A/cm^2]$

861     $C\frac{dV_i}{dt} = g_{Na}m^3h(V_{Na} - V_i) + g_Kn^4(V_K - V_i) + g_Aab(V_A - V_i) + g_hr(V_h - V_i)$

862     $+ g_L(V_L - V_i) + I_i + I_{cnst}$

863     $\frac{dx}{dt} = \frac{x_\infty(V) - x}{\tau_x(V)}$,   (Eq.2)

864   where $x = m$, h, n, a, b and r. The channel variables are determined by

865

866
$$x_\infty(V) = \frac{\alpha_x(V)}{\alpha_x(V) + \beta_x(V)},$$

867     $\tau_x(V) = \frac{1}{\alpha_x(V) + \beta_x(V)}$.

868   for m, h and n with

869
$$\alpha_m(V) = -\frac{0.1(V + 38)}{\exp\left(-\frac{v + 38}{10}\right) - 1}$$

870
$$\beta_m(V) = 4\exp\left(-\frac{V + 65}{18}\right)$$

871
$$\alpha_h(V) = 0.07\exp\left(-\frac{V + 63}{20}\right)$$

872
$$\beta_h(V) = 1/(\exp(-0.1(V + 33)) + 1)$$

873
$$\alpha_n(V) = \frac{0.018(V - 25)}{1 - \exp\left(-\frac{V - 25}{25}\right)}$$

874
$$\beta_n(V) = \frac{0.0036(V - 35)}{\exp\left(\frac{V - 35}{12}\right) - 1}$$

875 For $x = a$, b and r, variables in Eq.2 are determined by

876
$$a_\infty(V) = 1/(1 + \exp\left(-(V + 14)/16.6\right))$$

877
$$\tau_a(V) = 5$$

878
$$b_\infty(V) = 1/(1 + \exp\left((V + 71)/7.3\right))$$

879
$$\tau_b(V) = 1/(\frac{0.000009}{\exp\left(\frac{V - 26}{18.5}\right)} + \frac{0.014}{0.2 + \exp\left(-\frac{V + 70}{11}\right)})$$

880
$$r_\infty(V) = 1/(1 + \exp\left((V + 84)/10.2\right))$$

881
$$\tau_r(V) = 1/(\exp(-14.59 - 0.086V) + \exp\left(-1.87 + 0.0701V\right))$$

882

883 d) Excitatory neurons in MECIII

884 We modeled excitatory neurons in MECIII based on an excitatory neuron model of MECII

885 (S. Middleton et al., 2008), with some modifications of parameter values. These neurons

886 have an AHP current in addition to the standard sodium, potassium and leak currents.

887 The model is described as

888
$$V_{Na} = 50[mV], V_K = -90.0[mV], V_{AHP} = -100.0[mV], V_L = -65.0[mV]$$

889
$$g_{Na} = 100.0[mS/cm^2], g_K = 80.0[mS/cm^2], g_{AHP} = 0.3[mS/cm^2]$$

890
$$g_L = 0.5[mS/cm^2], C = 1.0[\mu F/cm^2].$$

891
$$C\frac{dV_i}{dt} = g_{Na}m^3h(V_{Na} - V_i) + g_Kn^4(V_K - V_i) + g_{AHP}w(V_{AHP} - V_i) + g_L(V_L - V_i) + I_i$$

892
$$\frac{dx}{dt} = \alpha_x(V)(1 - x) - \beta_x(V)x,$$

893 where $x = m$, n and h.

894
$$\alpha_m(V) = -0.32(V + 54)/(\exp\left(-0.25 * (V + 54)\right) - 1)$$

895
$$\beta_m(V) = 0.28(V + 27)/(\exp\left(0.2 * (V + 27)\right) - 1)$$

896
$$\alpha_n(V) = -0.032(V + 52)/(\exp\left(-0.2 * (V + 52)\right) - 1)$$

897
$$\beta_n(V) = 0.5\exp\left(-0.025(V + 57)\right)$$

898
$$\alpha_h(V) = 0.128\exp\left(-(V + 50)/18\right)$$

899
$$\beta_h(V) = 4.0/\exp\left(-0.2(V + 27) + 1\right).$$

900 The channel variable w is determined by

901
$$\frac{dw}{dt} = (w_\infty(V) - w)/\tau_w(V),$$

902
$$w_\infty(V) = \frac{1}{\exp\left(-0.1(V + 41)\right) + 1},$$

903
$$\tau_\infty(V) = \frac{500}{3.3\exp\left(0.05(V + 41)\right) + \exp\left(-0.05(V + 41)\right)}.$$

904

905 e) Excitatory neurons in MECV

906 Excitatory neurons in MECV are modeled based on (Egorov, Hamam, Fransen,
907 & Alonso, 2002; Fransén et al., 2006) with simplification of conductance of nonspecific
908 calcium-sensitive cationic, g_{CAN} (see Disinhibitory system in Materials and methods). Ca
909 flux is regulated through CaL channel.

910 $$V_{Na} = 50[mV], V_K = -100[mV], V_{CAN} = -20[mV], V_{Ca} = 140[mV], V_L = -65[mV]$$

911 $$g_{Na} = 100.0[mS/cm^2], g_K = 80.0[mS/cm^2], g_{AHP} = 0.05[mS/cm^2],$$

912 $$g_{K,C} = 195[mS/cm^2], g_M = 3.5[mS/cm^2], g_{CaL} = 0.15[mS/cm^2],$$

913 $$g_{Na,p} = 0.2[mS/cm^2], g_{K,A} = 0.5[mS/cm^2], g_L = 0.5[mS/cm^2],$$

914 $$C = 1.0[\mu F/cm^2]$$

915 $C\frac{dV_i}{dt} = g_{Na}m^3h(V_{Na} - V_i) + g_K n^4(V_K - V_i) + g_{AHP}w(V_{AHP} - V_i) + g_M s_M(V_K -$
916 $V_i) + g_{Na,p} s_{Na,p} h_{Na,p}(V_{Na} - V_i) + g_{K,A}s_{K,A}h_{K,A}(V_K - V_i) + g_{CAN}(t)s_{CAN}(V_{CAN} -$
917 $V_i) + g_{K,C} s_{KC}(V_K - V_i) + + g_{CaL}s_{CaL}(V_{Ca} - V_i) + I_i$ (Eq.3)

918 In addition to voltage dynamics, concentration of Ca^{2+}, $[Ca^{2+}]$, in a neuron is modeled
919 according to:

920 $$\frac{d[Ca^{2+}]}{dt} = \kappa I_{CaL} - [Ca^{2+}]/\tau_{Ca}$$

921 Here, $\kappa = 0.5181937[Fd^{-1}]$ and $\tau_{Ca} = 250[ms]$.

922 The standard current of sodium and potassium in Eq.3 are exactly same as in excitatory
923 neurons in MECIII. AHP, KA, KC, M, Na_p and CaL currents follow the standard activation-
924 inactivation forms:

925 $$\frac{dx}{dt} = \alpha_x(V)(1 - x) - \beta_x(V)x$$

926 $x = w(= AHP), s_M(= M), s_{K,A}, h_{K,A}, s_{K,C}(= KC), s_{CaL}(= CaL)$.

927 α and β of each current are according to the following equations.:

928 $$\alpha_{AHP}(V) = \begin{cases} \min(2.4([Ca^{2+}] - 15), 15) & \text{for } [Ca^{2+}] > 15 \\ 0.2[Ca^{2+}] & \text{otherwise} \end{cases}$$

929 $$\beta_{AHP}(V) = 1$$

930 $$\alpha_{CaL}(C) = \frac{1.6}{1 + \exp(-0.072(V - 65))}$$

931 $$\beta_{CaL}(V) = \frac{0.02(V - 51.1)}{\exp(0.2(V - 51.1)) - 1}$$

932 $$\alpha_{KC}(V) = \begin{cases} \dfrac{\exp(0.053782V - 0.66835)}{18.975} & \text{for } V < 50 \\ 2\exp\left(\dfrac{6.5 - V}{27}\right) & \text{otherwise} \end{cases}$$

933 $$\beta_{KC}(V) = \begin{cases} 2\exp\left(\dfrac{6.5 - V}{27}\right) - \alpha_{KC} & \text{for } V < 50 \\ 0 & \text{otherwise} \end{cases}$$

934
$$\alpha_{s_{KA}}(V) = \frac{0.02(V - 13.1)}{1 - \exp(0.1(13.1 - V))}$$

935
$$\beta_{s_{KA}}(V) = \frac{0.175(V - 40.1)}{\exp(0.1(V - 40.1)) - 1}$$

936
$$\alpha_{h_{KA}}(V) = 0.0016\exp(-(V + 13)/18)$$

937
$$\beta_{h_{KA}}(V) = 0.05/(1 + 0.2\exp(10.1 - V))$$

938 Variables for M, Na$_p$ and CAN channels follow the form:

939
$$\frac{dx}{dt} = \frac{x_\infty(V) - x}{\tau_x(V)},$$

940 where $x = s_{Na,p}, h_{Na,p}, s_M (= M), s_{CAN} (= CAN)$. x_∞ and τ_x for each variable are

941 according to

942
$$s_{M,\infty}(V) = 1/(1 + \exp(-V + 35)/5)$$

943
$$\tau_M(V) = \frac{1000}{3.3\exp((V + 35)/40) + \exp(-(V + 35)/20)}$$

944
$$s_{Na,p\infty}(V) = 1/(1 + \exp\left(-\frac{V + 48.7}{4.4}\right))$$

945
$$\tau_{s_{Nap}}(V) = \frac{1}{\left(\frac{0.091(V + 38)}{1 - \exp\left(\frac{V + 38}{5}\right)} - \frac{0.062(V + 38)}{1 - \exp\left(\frac{V + 38}{5}\right)}\right)}$$

946
$$h_{Na,p\infty}(V) = \frac{1}{1 + \exp\left(-\frac{V + 48.8}{9.98}\right)}$$

947
$$\tau_{h_{Na,p}}(V) = \frac{1}{-\frac{0.00000288(V - 49.1)}{1 - \exp\left(-\frac{V - 49.1}{4.63}\right)} + -\frac{0.00000694(V + 44.7)}{1 - \exp\left(-\frac{V + 44.7}{2.63}\right)}}$$

948
$$s_{CAN,\infty}(V) = 48 \times \frac{10^2[Ca^{2+}]^2}{48 \times 10^2[Ca^{2+}]^2 + 0.03}$$

949
$$\tau_{s_{CAN}}(V) = 1/(48 \times 10^2[Ca^{2+}]^2).$$

950

951

952

953 **Synaptic Inputs**

954 Synaptic input I_i to neuron *i* includes excitatory I_i^E and inhibitory I_i^I currents. Only in CA1

955 neurons, OLM currents, which are from OLM neurons, are modeled as another type of

956 inhibitory currents based on (Wulff et al., 2009).

957
$$I_i(t) = I_i^E + I_i^I = g_i^E(V_E - V) + g_i^I(V_I - V) + g_i^{OLM}(V_i - V)$$

958
$$g_i^{E,I,OLM}(t) = \Sigma_k \int_0^t G_{ik}\Sigma_s \alpha^{E,I,OLM}(t' - t_k^s - d_{ik})dt' \text{ (Eq.4)},$$

33

959 where k is index of pre-synaptic neuron. For the excitatory current, k corresponds to
960 index of excitatory neurons in all cortical areas and excitatory noise neurons projecting
961 to post-synaptic neuron *i*. For the inhibitory currents, *k* corresponds to index of
962 inhibitory neurons (PV, OLM, VIP, GABA) in all cortical areas and inhibitory noise neurons
963 projecting to post-synaptic neuron *i* . Connections *G* among these neurons are described
964 in Circuit model in Materials and Methods. *s* is index of spikes in *k* neuron. d_{ik} is
965 transduction time lag. When neurons *i* and *k* are within a same area, *d* is chosen
966 randomly from (0,2) ms, while *d* is chosen from (10,15) ms for neurons in different areas.
967 Double exponential functions, α, are described as:

968 $\alpha^{E,I,OLM}(t) = (e^{-\frac{t}{\tau^r_{E,I,OLM}}} - e^{-\frac{t}{\tau^d_{E,I,OLM}}})/(\tau^r_{E,I,OLM} - \tau^d_{E,I,OLM})$ (Eq.5)

969 Rise time constant t^r is 0.05,0.07 and 2.0 ms for E, I, and OLM, respectively, while decay
970 time constant t^d is 5.3, 9.1 and 22.0 ms for E, I, and OLM, respectively.

971

972

973 **Circuit structure**

974 Our model has three cortical areas (Figure1A) and external oscillating neurons in MECII,
975 CA3 and MS. excitatory neurons in each cortical area are divided into two or four
976 subgroups (Table1). CA1 has four groups denoted as Left (L), Right (R), Center (C) and
977 Home (H). MECIII and MECV have two groups denoted as L and R.

978

979 Table1: number of neurons in each are

	CA1	ECIII	ECV	CA3
E	120x4	120x2	200x2	120x4
PV	240	160	120	
OLM	240			

980

981

982 In addition, a model has 240 VIP neurons in CA1, 120 excitatory neurons in MECII and
983 360 GABAergic neurons in MS. The GABAergic neurons are divided into three groups
984 projecting to different types of neuron each of which has 120 neurons; groups to OLM,
985 to PV in CA1 and to PV in MECV.
986 Structure of a circuit is given by a matrix *G* in Eq. 4, which represents efficacy of synaptic
987 connections. Connection between presynaptic neuron *j* and postsynaptic neuron *I*, G_{ij}
988 is determined by

989 $G_{ij} = \begin{cases} G^{AB}_{XY}/\rho^{AB}_{XY} N^B_Y & \text{with probability } \rho^{AB}_{XY} \\ 0 & \text{otherwise} \end{cases}$ (Eq.6),

34

990 where X and Y are neuron types that i and j neurons belong to, respectively. A and B
991 refer subgroups (L,R,C,and H) that i and j neurons belong to, respectively. Because only
992 excitatory neurons in each area are divided as the subgroups, A and B are neglected for
993 other types of neurons. N_Y is the number of type Y neurons. If the type Y neurons are
994 divided into the subgroup, N^B_Y indicates the number of type Y neurons in subgroup B. G
995 and ρ for each connection are as follows:
996
997 i) Connection from noise neurons
998 Connections G from noise neurons to the neurons in cortical areas are shown in Table2.
999 A postsynaptic neuron receives inputs from 40 excitatory and 40 inhibitory neurons
1000 $(\rho_{XY} = 1, N_{XY} = 40)$.
1001
1002 Table2 Connection G_{XY} from noise neurons to each type of neurons.

Post–synaptic X \ Pre–synaptic Y	CA1			ECIII		ECV	
	E	PV	OLM	E	PV	E	PV
Excitatory noise neurons	.32	.8	3.2	.8	.2	.2	.4
Inhibitory noise neurons	.6	.2	.4	.6	.8	.2	.6

1003
1004
1005 ii) Connection from excitatory neurons in MECII, MS and CA3
1006 a) connection from excitatory neurons in MECII to PV in MECIII
1007
$$G_{XY} = 0.4$$
1008
$$\rho_{XY} = 1$$
1009 b) from GABAergic neurons in MS
1010 to PV in MECV
1011
$$G_{XY} = 0.1$$
1012 to PV in CA1
1013
$$G_{XY} = 3.7$$
1014 to OLM in CA1
1015
$$G_{XY} = 3.7$$
1016 For all connections,
1017
$$\rho_{XY} = 1$$
1018 c) from CA3 to E in CA1
1019 for $A \neq B$
1020
$$G_{XY}^{AB} = 0, \rho_{XY}^{AB} = 0$$
1021 For $A = B$
1022
$$G_{XY}^{AB} = 2.0\xi, \rho_{XY}^{AB} = 0.3$$

35

1023   here, ξ is chosen randomly from (0,1).

1024   d) from CA3 to PV in CA1

1025 $G_{XY} = 0.1 \; \rho_{XY} = 0.5$.

1026   e) from VIP to PV and OLM in CA1

1027   Efficacy of these connections is modified by [ACh] (Tremblay, Lee, & Rudy, 2016) as

1028   follows:

1029   For X=PV,

1030
$$G_{XY} = 0.012[Ach], \rho_{XY} = 1$$

1031   For X=OLM,

1032
$$G_{XY} = 0.02[Ach], \; \rho_{XY} = 1$$

1033   f) Connections between E neurons within the same cortical areas

1034   For $A \neq B$

1035
$$G_{XY}^{AB} = 0.01, \rho = 0.025 \text{ (in MECIII)}$$

1036
$$G_{XY}^{AB} = 0, \rho = 0 \text{ (in MECV)}$$

1037   For $A = B$

1038
$$G_{XY}^{AB} = 14.4, \rho = 0.15 \text{ (in MECIII)}$$

1039
$$G_{XY}^{AB} = 0.216, \rho = 0.03 \text{ (in MECV)}$$

1040   There is no connection between excitatory neurons in CA1 in our model.

1041

1042   g) Connection between neurons within the same cortical areas (except E-E connections)

1043   There is no connection between OLMs(Wulff et al., 2009). Connections from OLM to E

1044   neurons in CA1 are described in h), since OLM is observed to be attached on proximal

1045   dendrite of excitatory neurons in CA1 and regulate inputs from MECIII.

1046

1047   Other connections within cortical areas are shown in Table 3.

1048

1049   Table 3: connection parameters in CA1, MECIII, MECV

	CA1					
(X,Y)	E,PV	PV,E	PV,PV	PV,OLM	OLM,E	OLM,PV
G_{XY}	2.2	0.2	0.3	0.5	0.5	0.2
ρ_{XY}	0.5	0.5	0.5	0.5	0.3	0.5

1050

MECIII			MECV		
E,PV	PV,E	PV,PV	E,PV	PV,E	PV,PV
2.5	0.5	0.01	0.2	0.3	0.01

0.5	0.3	0.3	0.5	0.3	0.3

1051

1052   h) connections from neurons in CA1 to those in MECV

1053   For X=excitatory neurons in MECV, Y=excitatory neurons in CA1,

1054 $$G_{XY}^{AB} = \begin{cases} 0.27 & \text{for } B \in \{H, C\} \\ 0.36 & \text{for } (A, B) \in \{(L,L),(R,R)\} \\ 0.00125 & \text{otherwise} \end{cases}, \rho_{XY}^{AB} = \begin{cases} 0.075 & \text{for } B \in \{H, C\} \\ 0.075 & \text{for } (A, B) \in \{(L,L),(R,R)\} \\ 0.0125 & \text{otherwise} \end{cases}$$

1055   For X=PV neurons in MECV, Y=excitatory neurons in CA1,

1056 $$G_{XY} = 0.01, \qquad \rho_{XY} = 0.3$$

1057

1058   i) connections from neurons in MECV to those in MECIII

1059   For X= excitatory neurons in MECIII, Y=excitatory neurons in MECV,

1060 $$G_{XY}^{AB} = \begin{cases} 0.01 & \text{for } A \neq B \\ 1.44 & \text{otherwise} \end{cases}, \rho_{XY}^{AB} = \begin{cases} 0.0125 & \text{for } A \neq B \\ 0.075 & \text{otherwise} \end{cases}$$

1061

1062   j) connections from neurons in MECIII to those in CA1

1063   For X=excitatory neurons in CA1, Y=excitatory neurons in MECIII,

1064 $$G_{XY}^{AB} = \begin{cases} 0.003 & \text{for } A \neq B \\ 0.216 & \text{otherwise} \end{cases}, \rho_{XY}^{AB} = \begin{cases} 0.01 & \text{for } A \neq B \\ 0.06 & \text{otherwise} \end{cases}$$

1065   In addition, effect of OLM is implemented for modulating inputs from MECIII as follows:

1066   Up to 5 ms after a spike from OLM to E neurons in CA1, efficacy of connections from E

1067   neurons in MECIII to this E neurons in CA1 is reduced with multiplication by 0.1.

1068

1069

1070   **Nonlinear interaction of excitatory neurons in CA1 with input from MECIII and CA3**

1071   E neurons integrate spikes from CA3 and MECIII (Bittner et al., 2015). We introduced

1072   this effect in our model. A prolonged EPSC I_{prol} is supposed to be generated, when the

1073   following conditions are satisfied:

1074   ●   An excitatory neuron in CA1 receives a burst (three spikes within 15ms) from MECIII

1075   and it does not receive any inhibitory input from OLM within 15ms at time t_1.

1076   ●   This excitatory CA1 receives a burst (three spikes within 10ms) from CA3 within

1077   20ms from t_1 (denoted t_2).

1078   ●   Previous prolonged EPSC is 100ms earlier than t_2.

1079   If these conditions are satisfied, a prolonged (100ms) EPSC in E neuron in CA1 is

1080   generated according to:

1081
$$\alpha_{prol}(t) = \begin{cases} \dfrac{t}{5} & \text{for } 0 < t < 5[ms] \\ 1 - \dfrac{t-5}{60} & \text{for } 5 < t < 35 \\ 0.5\exp\left(-\dfrac{t-35}{30}\right) & \text{for } 35 < t < 100 \\ 0 & \text{otherwise} \end{cases}$$

1082
$$I_{prol}(t) = 0.01\alpha_{prol}(t)$$

1083

1084

1085 **Disinhibitory system and modulated conductance of nonspecific calcium-sensitive**
1086 **cationic (CAN) current through ACh.**

1087 We assume that concentration of ACh represents cognitive states and changes
1088 dependent of current locations:

1089
$$[ACh] = \begin{cases} 0.2 & \text{for } t < 1[s] \text{ (a rat on sample-C)} \\ 1 - 0.8\exp\left(-\dfrac{t-T_{LS}}{200}\right) & \text{for } 1[s] \le t < 3[s] \text{ (a rat on sample-L)} \\ 0.8 - 0.2\exp\left(-\dfrac{t-T_H}{200}\right) & \text{for } 3[s] \le t < 4.5[s] \text{ (a rat on sample-L)} \\ 1.1 - 0.3\exp\left(-\dfrac{t-T_{CT}}{200}\right) & \text{for } 4.5[s] \le t \text{ (a rat on test-C)} \end{cases}$$

1090 [ACh] modifies neural behavior in a circuit in two pathways. Efficacy of connections from
1091 VIP is modified with [ACh] (Circuit structure in Materials and methods) as well as
1092 conductance of I_{CAN}. A channel of I_{CAN} takes high and low conductance states
1093 alternatively. Maximum conductance g_{CAN} is determined by [ACh] and ratio of high
1094 conductance state r_h. r_h is dependent on history of [Ca2+] and [ACh] (Fransén et al.,
1095 2006) as follows:

1096
$$g_{CAN}(t) = 0.5[Ach]r_h(t)$$

1097
$$r_h(t + \Delta t) = \begin{cases} r_h(t) + 0.6\Delta t & \text{for } [Ca^{2+}] > 0.004 \\ r_h(t) - 0.08\Delta t & \text{for } [Ca^{2+}] < 0.0003 \\ r_h(t) & \text{otherwise} \end{cases}$$

1098 We also set upper and lower bounds for r_h at 1 and 0.12, respectively.

1099

1100

1101 **Periodicity analysis**

1102 Neural activity in the model oscillates driven by external theta rhythm (10Hz). We
1103 evaluated how strongly neurons oscillate in the theta rhythm by calculating an
1104 autocorrelation function R(t) (Yamamoto et al., 2014). Periodicity index is defined as
1105 $\displaystyle \max_{50ms < t < 200ms} R(t).$

1106

1107

Experimental data in rodents

Spiking activities and LFP data in CA1 are obtained from previously published data in (Yamamoto et al., 2014) for Figures 6B and 7C and that in (Mizuseki et al., 2013) for Figures 6D and 6E. Experiments were approved by the Institutional Animal Care and Use Committee of Rutgers University. All procedures for animal care and use were performed in accordance with the National Institutes of Health Guide for the Care and Use of Laboratory Animals. Detailed conditions on data recording are described in these papers.

LFP activities were band-pass filtered (6-12Hz) as theta wave and instantaneous phase of the filtered theta wave were derived from Hilbert transform. For spiking activities, we dropped a part of spikes to analyzed as follows:
Spiking activities in (Yamamoto et al., 2014) were recorded with the silicon linear probes and were analyzed as multi-unit activities. In this paper, however, we roughly distinguish putative excitatory neurons from inhibitory ones in order to show clear theta preference. According to (Mizuseki et al., 2009), we sorted spikes by trough to peak latency. Due to short length of single spike profile in the data, we cannot identify baseline before spike and consequently cannot compute peak amplitude asymmetry. We assigned spikes with the latency larger than 0.5ms to putative excitatory neurons. For Figure 6B, we have the sorted spikes in three out of five rats because spikes of the rest two rats do not show clear theta preference due to small number of spikes.
For spiking activities in (Mizuseki et al., 2013), we used sessions "ec014.12","ec014.16","ec014.17","ec014.27","ec014.28","ec013.44","ec013.46","ec016.30". Because phase shift in the side arm was observed only in deeper neurons in (Fernández-Ruiz et al., 2017), we only used spikes of deeper neurons according to (Mizuseki, Diba, Pastalkova, & Buzsáki, 2011).

Calculations of the ratio of spikes at the peaks in theta and the side-to-center ratio

In Figure 6F, we used the same neurons in Figure 6E (see Experimental data in rodents). Further, we filtered these neurons by two criteria: i) number of spikes in the later center arm are larger than 50; ii) the ratio of spikes in the later center arm to total spikes is larger than 5%. To exclude place cells representing the earlier center arm and junction of T-maze (since these cells are likely to spike at the peaks in theta oscillation in the later center arm), we further excluded the cells that spike in the later center arm less frequently than at the earlier center arm or at the junction. Eleven neurons remained. For these neurons, we calculated the ratio in number of spikes around the peaks (90-270 degree) to all spikes in the later center arm. We call this quantity the ratio of spikes at the peaks. We also calculated the ratio of average number of spikes emitted in the

39

1146   later center arm to that of average number of spikes emitted in the side arms. We call

1147   this quantity the side-to-center ratio.

1148

1149   **Data and Software Availability**

1150   The computer codes used to generate the present simulation results will be available

1151   upon request.

1152   **Acknowledgement**

1153   We thank Jun Yamamoto for providing experimental data and fruitful discussion and

1154   György Buzsáki for publicly sharing the valuable data. This work was supported by

1155   KAKENHI (nos. 18H05213, 18K15343 and 19H04994) from the MEXT, Japan.

1156

1157   **Declaration of Interests**

1158   The authors declare no competing interests.

1159

1160

1161   **References**

1162   Akam, T. E., & Kullmann, D. M. (2010). Oscillations and Filtering Networks Support
1163   Flexible Routing of Information. *Neuron*, *67*(2), 308–320.
1164   https://doi.org/10.1016/j.neuron.2010.06.019

1165   Albuquerque, E. X., Pereira, E. F. R., Alkondon, M., & Rogers, S. W. (2009). Mammalian
1166   Nicotinic Acetylcholine Receptors: From Structure to Function. *Physiological*
1167   *Reviews*, *89*(1), 73–120. https://doi.org/10.1152/physrev.00015.2008

1168   Bell, L. A., Bell, K. a, & McQuiston, a R. (2014). Activation of muscarinic receptors by
1169   ACh release in hippocampal CA1 depolarizes VIP but has varying effects on
1170   parvalbumin-expressing basket cells. *The Journal of Physiology*, *1*, 197–215.
1171   https://doi.org/10.1113/jphysiol.2014.277814

1172   Benchenane, K., Peyrache, A., Khamassi, M., Tierney, P. L., Gioanni, Y., Battaglia, F. P.,
1173   & Wiener, S. I. (2010). Coherent Theta Oscillations and Reorganization of Spike
1174   Timing in the Hippocampal- Prefrontal Network upon Learning. *Neuron*, *66*(6),
1175   921–936. https://doi.org/10.1016/j.neuron.2010.05.013

1176   Bittner, K. C., Grienberger, C., Vaidya, S. P., Milstein, A. D., Macklin, J. J., Suh, J., …
1177   Magee, J. C. (2015). Conjunctive input processing drives feature selectivity in
1178   hippocampal CA1 neurons. *Nature Neuroscience*, *18*(July), 1–13.
1179   https://doi.org/10.1038/nn.4062

1180   Bolkan, S. S., Stujenske, J. M., Parnaudeau, S., Spellman, T. J., Rauffenbart, C., Abbas, A.
1181   I., … Kellendonk, C. (2017). Thalamic projections sustain prefrontal activity during
1182   working memory maintenance. *Nature Neuroscience*, *20*(7), 987–996.
1183   https://doi.org/10.1038/nn.4568

1184 Borhegyi, Z. (2004). Phase Segregation of Medial Septal GABAergic Neurons during
1185   Hippocampal Theta Activity. *Journal of Neuroscience*, *24*(39), 8470–8479.
1186   https://doi.org/10.1523/JNEUROSCI.1413-04.2004

1187 Buehlmann, A., & Deco, G. (2010). Optimal Information Transfer in the Cortex through
1188   Synchronization. *PLoS Computational Biology*, *6*(9), e1000934.
1189   https://doi.org/10.1371/journal.pcbi.1000934

1190 Colgin, L. L., Denninger, T., Fyhn, M., Hafting, T., Bonnevie, T., Jensen, O., … Moser, E. I.
1191   (2009). Frequency of gamma oscillations routes flow of information in the
1192   hippocampus. *Nature*, *462*(7271), 353–357. https://doi.org/10.1038/nature08573

1193 Croxson, P. L., Kyriazis, D. A., & Baxter, M. G. (2011). Cholinergic modulation of a
1194   specific memory function of prefrontal cortex. *Nature Neuroscience*, *14*(12),
1195   1510–1512. https://doi.org/10.1038/nn.2971

1196 Cutsuridis, V., Cobb, S., & Graham, B. P. (2010). Encoding and retrieval in a model of
1197   the hippocampal CA1 microcircuit. *Hippocampus*, *20*(3), 423–446.
1198   https://doi.org/10.1002/hipo.20661

1199 Dolleman-Van Der Weel, M., & Witter, M. P. (1996). Projections From the Nucleus
1200   Reuniens Thalami to the Entorhinal Cortex , Hippocampal Field CA1 , and the
1201   Subiculum in the Rat Arise From Different Populations of Neurons. *The Journal of*
1202   *Comparative Neurology*, *364*, 637–650.

1203 Donato, F., Rompani, S. B., & Caroni, P. (2013). Parvalbumin-expressing basket-cell
1204   network plasticity induced by experience regulates adult learning. *Nature*,
1205   *504*(7479), 272–276. https://doi.org/10.1038/nature12866

1206 Dragoi, G., & Buzsáki, G. (2006). Temporal encoding of place sequences by
1207   hippocampal cell assemblies. *Neuron*, *50*(1), 145–157.
1208   https://doi.org/10.1016/j.neuron.2006.02.023

1209 Durstewitz, D., Vittoz, N. M., Floresco, S. B., & Seamans, J. K. (2010). Abrupt transitions
1210   between prefrontal neural ensemble states accompany behavioral transitions
1211   during rule learning. *Neuron*, *66*(3), 438–448.
1212   https://doi.org/10.1016/j.neuron.2010.03.029

1213 Egorov, a V, Hamam, B. N., Fransen, E., Hasselmo, M. E., & Alonso, A. A. (2002).
1214   Graded persistent activity in entorhinal cortex neurons. *Nature*, *420*(6912), 173–
1215   178. https://doi.org/10.1038/nature01030.1.

1216 Eichenbaum, H. (2017). Prefrontal – hippocampal interactions in episodic memory.
1217   *Nature Review Neurosci*, *18*(9), 547–558. https://doi.org/10.1038/nrn.2017.74

1218 Ferbinteanu, J., & Shapiro, M. L. (2003). Prospective and Retrospective Memory Coding
1219   in the Hippocampus. *Neuron*, *40*(6), 1227–1239. https://doi.org/10.1016/S0896-
1220   6273(03)00752-9

1221 Fernández-Ruiz, A., Oliva, A., Nagy, G. A., Maurer, A. P., Berényi, A., & Buzsáki, G.
1222   (2017). Entorhinal-CA3 Dual-Input Control of Spike Timing in the Hippocampus by
1223   Theta-Gamma Coupling. *Neuron*, *93*(5), 1213-1226.e5.
1224   https://doi.org/10.1016/j.neuron.2017.02.017

1225 Foster, D. J., & Wilson, M. A. (2006). Reverse replay of behavioural sequences in
1226   hippocampal place cells during the awake state. *Nature*, *440*(7084), 680–683.
1227   https://doi.org/10.1038/nature04587

1228 Francavilla, R., Villette, V., Luo, X., Chamberland, S., Muñoz-Pino, E., Camiré, O., …
1229   Topolnik, L. (2018). Connectivity and network state-dependent recruitment of
1230   long-range VIP-GABAergic neurons in the mouse hippocampus. *Nature*
1231   *Communications*, *9*(1), 5043. https://doi.org/10.1038/s41467-018-07162-5
1232 Fransen, E., Alonso, A. A., & Hasselmo, M. E. (2002). Simulations of the role of the
1233   muscarinic-activated calcium-sensitive nonspecific cation current INCM in
1234   entorhinal neuronal activity during delayed matching tasks. *The Journal of*
1235   *Neuroscience : The Official Journal of the Society for Neuroscience*, *22*(3), 1081–
1236   1097. Retrieved from http://www.ncbi.nlm.nih.gov/pubmed/11826137
1237 Fransén, E., Tahvildari, B., Egorov, A. V, Hasselmo, M. E., & Alonso, A. a. (2006).
1238   Mechanism of graded persistent cellular activity of entorhinal cortex layer v
1239   neurons. *Neuron*, *49*(5), 735–746. https://doi.org/10.1016/j.neuron.2006.01.036
1240 Fries, P. (2015). Rhythms for Cognition: Communication through Coherence. *Neuron*,
1241   *88*(1), 220–235. https://doi.org/10.1016/j.neuron.2015.09.034
1242 Furey, M. L., Pietrini, P., & Haxby, J. V. (2000). Cholinergic enhancement and increased
1243   selectivity of perceptual processing during working memory. *Science (New York,*
1244   *N.Y.)*, *290*(5500), 2315–2319. https://doi.org/10.1126/science.290.5500.2315
1245 Gonzalez-Sulser, A., Parthier, D., Candela, A., McClure, C., Pastoll, H., Garden, D., …
1246   Nolan, M. F. (2014). GABAergic Projections from the Medial Septum Selectively
1247   Inhibit Interneurons in the Medial Entorhinal Cortex. *Journal of Neuroscience*,
1248   *34*(50), 16739–16743. https://doi.org/10.1523/JNEUROSCI.1612-14.2014
1249 Guise, K. G., & Shapiro, M. L. (2017). Medial Prefrontal Cortex Reduces Memory
1250   Interference by Modifying Hippocampal Encoding. *Neuron*, *94*(1), 183-192.e8.
1251   https://doi.org/10.1016/j.neuron.2017.03.011
1252 Gupta, A. S., van der Meer, M. A. A., Touretzky, D. S., & Redish, A. D. (2010).
1253   Hippocampal Replay Is Not a Simple Function of Experience. *Neuron*, *65*(5), 695–
1254   705. https://doi.org/10.1016/j.neuron.2010.01.034
1255 Hangya, B., Ranade, S. P., Lorenc, M., & Kepecs, A. (2015). Central Cholinergic Neurons
1256   Are Rapidly Recruited by Reinforcement Feedback. *Cell*, *162*(5), 1155–1168.
1257   https://doi.org/10.1016/j.cell.2015.07.057
1258 Hasselmo, M. E. (2006). The role of Acetylcholine in learning and memory. *Current*
1259   *Opinion in Neurobiology*, *16*. https://doi.org/10.1016/j.conb.2006.09.002
1260 Hasselmo, M. E., Bodelón, C., & Wyble, B. P. (2002). A proposed function for
1261   hippocampal theta rhythm: separate phases of encoding and retrieval enhance
1262   reversal of prior learning. *Neural Computation*, *14*(4), 793–817.
1263   https://doi.org/10.1162/089976602317318965
1264 Hasselmo, M. E., & Sarter, M. (2010). Modes and Models of Forebrain Cholinergic
1265   Neuromodulation of Cognition. *Neuropsychopharmacology*, *36*(1), 52–73.
1266   https://doi.org/10.1038/npp.2010.104
1267 Hasselmo, M. E., & Stern, C. E. (2006). Mechanisms underlying working memory for
1268   novel information. *Trends in Cognitive Sciences*, *10*(11), 487–493.
1269   https://doi.org/10.1016/j.tics.2006.09.005

Ito, H. T., Zhang, S., Witter, M. P., Moser, E. I., & Moser, M. (2015). A prefrontal–thalamo–hippocampal circuit for goal-directed spatial navigation. *Nature*, *522*(7554), 50–55. https://doi.org/10.1038/nature14396

Jones, M. W., & Wilson, M. A. (2005). Theta Rhythms Coordinate Hippocampal–Prefrontal Interactions in a Spatial Memory Task. *PLoS Biology*, *3*(12), e402. https://doi.org/10.1371/journal.pbio.0030402

Kamigaki, T., & Dan, Y. (2017). Delay activity of specific prefrontal interneuron subtypes modulates memory-guided behavior. *Nature Neuroscience*, *20*(6), 854–863. https://doi.org/10.1038/nn.4554

Kitamura, T., Pignatelli, M., Suh, J., Kohara, K., Yoshiki, A., Abe, K., & Tonegawa, S. (2014). Island Cells Control Temporal Association Memory. *Science, 343*(6173), 896–901. https://doi.org/10.1126/science.1244634

Klausberger, T., & Somogyi, P. (2008). Neuronal diversity and temporal dynamics: the unity of hippocampal circuit operations. *Science (New York, N.Y.)*, *321*(5885), 53–57. https://doi.org/10.1126/science.1149381

Lasztóczi, B., & Klausberger, T. (2016). Hippocampal Place Cells Couple to Three Different Gamma Oscillations during Place Field Traversal. *Neuron*, *91*(1), 34–40. https://doi.org/10.1016/j.neuron.2016.05.036

Letzkus, J. J., Wolff, S. B. E., & Lüthi, A. (2015). Disinhibition, a Circuit Mechanism for Associative Learning and Memory. *Neuron*, *88*(2), 264–276. https://doi.org/10.1016/j.neuron.2015.09.024

Letzkus, J. J., Wolff, S. B. E., Meyer, E. M. M., Tovote, P., Courtin, J., Herry, C., & Lüthi, A. (2011). A disinhibitory microcircuit for associative fear learning in the auditory cortex. *Nature*, *480*(7377), 331–335. https://doi.org/10.1038/nature10674

McGaughy, J., Koene, R. A., Eichenbaum, H., & Hasselmo, M. E. (2005). Cholinergic Deafferentation of the Entorhinal Cortex in Rats Impairs Encoding of Novel But Not Familiar Stimuli in a Delayed Nonmatch-to-Sample Task. *J. Neurosci.*, *25*(44), 10273–10281. https://doi.org/10.1523/JNEUROSCI.2386-05.2005

Middleton, S. J., & McHugh, T. J. (2016). Silencing CA3 disrupts temporal coding in the CA1 ensemble. *Nature Neuroscience*, *19*(7), 945–951. https://doi.org/10.1038/nn.4311

Middleton, S., Jalics, J., Kispersky, T., Lebeau, F. E. N., Roopun, A. K., Kopell, N. J., … Cunningham, M. O. (2008). NMDA receptor-dependent switching between different gamma rhythm-generating microcircuits in entorhinal cortex. *Proceedings of the National Academy of Sciences of the United States of America*, *105*(47), 18572–18577. https://doi.org/10.1073/pnas.0809302105

Milstein, A. D., Bloss, E. B., Apostolides, P. F., Vaidya, S. P., Dilly, G. A., Zemelman, B. V, & Magee, J. C. (2015). Inhibitory Gating of Input Comparison in the CA1 Microcircuit. *Neuron*, *87*(6), 1274–1289. https://doi.org/10.1016/j.neuron.2015.08.025

Mizuseki, K., Diba, K., Pastalkova, E., & Buzsáki, G. (2011). Hippocampal CA1 pyramidal cells form functionally distinct sublayers. *Nature Neuroscience*, *14*(9), 1174-. https://doi.org/10.1038/nn.2894.Hippocampal

43

1313 Mizuseki, K., Sirota, A., Pastalkova, E., & Buzsáki, G. (2009). Theta Oscillations Provide
1314   Temporal Windows for Local Circuit Computation in the Entorhinal-Hippocampal
1315   Loop. *Neuron*, *64*(2), 267–280. https://doi.org/10.1016/j.neuron.2009.08.037
1316 Mizuseki, K., Sirota, A., Pastalkova, E., Diba, K., & Buzsaki, G. (2013). Multiple single
1317   unit recordings from different rat hippocampal and entorhinal regions while the
1318   animals were performing multiple behavioral tasks. *CRCNS.Org*.
1319   https://doi.org/10.6080/K09G5JRZ
1320 Mongillo, G., Barak, O., & Tsodyks, M. (2008). Synaptic theory of working memory.
1321   *Science (New York, N.Y.)*, *319*(5869), 1543–1546.
1322   https://doi.org/10.1126/science.1150769
1323 Muñoz, W., Tremblay, R., Levenstein, D., & Rudy, B. (2017). Layer-specific modulation
1324   of neocortical dendritic inhibition during active wakefulness. *Science*, *355*(6328),
1325   954–959. https://doi.org/10.1126/science.aag2599
1326 Murray, A. J., Sauer, J.-F., Riedel, G., McClure, C., Ansel, L., Cheyne, L., … Wulff, P.
1327   (2011). Parvalbumin-positive CA1 interneurons are required for spatial working
1328   but not for reference memory. *Nature Neuroscience*, *14*(3), 297–299.
1329   https://doi.org/10.1038/nn.2751
1330 Murray, J. D., Bernacchia, A., Roy, N. A., Constantinidis, C., Romo, R., & Wang, X.-J.
1331   (2017). Stable population coding for working memory coexists with
1332   heterogeneous neural dynamics in prefrontal cortex. *Proceedings of the National*
1333   *Academy of Sciences*, *114*(2), 394–399. https://doi.org/10.1073/pnas.1619449114
1334 Newman, E. L., Gupta, K., Climer, J. R., Monaghan, C. K., & Hasselmo, M. E. (2012).
1335   Cholinergic modulation of cognitive processing: insights drawn from
1336   computational models. *Frontiers in Behavioral Neuroscience*, *6*(June), 1–19.
1337   https://doi.org/10.3389/fnbeh.2012.00024
1338 O'Keefe, J., & Dostrovsky, J. (1971). The hippocampus as a spatial map. Preliminary
1339   evidence from unit activity in the freely-moving rat. *Brain Research*, *34*(1), 171–
1340   175. https://doi.org/10.1016/0006-8993(71)90358-1
1341 Okada, K., Nishizawa, K., Kobayashi, T., Sakata, S., & Kobayashi, K. (2015). Distinct roles
1342   of basal forebrain cholinergic neurons in spatial and object recognition memory.
1343   *Scientific Reports*, *5*(1), 13158. https://doi.org/10.1038/srep13158
1344 Palmigiano, A., Geisel, T., Wolf, F., & Battaglia, D. (2017). Flexible information routing
1345   by transient synchrony. *Nature Neuroscience*, *20*(7), 1014–1022.
1346   https://doi.org/10.1038/nn.4569
1347 Parikh, V., Kozak, R., Martinez, V., & Sarter, M. (2007). Prefrontal Acetylcholine Release
1348   Controls Cue Detection on Multiple Timescales. *Neuron*, *56*(1), 141–154.
1349   https://doi.org/10.1016/j.neuron.2007.08.025
1350 Pastalkova, E., Itskov, V., Amarasingham, A., & Buzsaki, G. (2008). Internally Generated
1351   Cell Assembly Sequences in the Rat Hippocampus. *Science*, *321*(5894), 1322–
1352   1327. https://doi.org/10.1126/science.1159775
1353 Pfeiffer, B. E., & Foster, D. J. (2013). Hippocampal place-cell sequences depict future
1354   paths to remembered goals. *Nature*, *497*(7447), 74–79.
1355   https://doi.org/10.1038/nature12112

Pi, H.-J., Hangya, B., Kvitsiani, D., Sanders, J. I., Huang, Z. J., & Kepecs, A. (2013). Cortical interneurons that specialize in disinhibitory control. *Nature*, *503*(7477), 521–524. https://doi.org/10.1038/nature12676

Pinto, L., Goard, M. J., Estandian, D., Xu, M., Kwan, A. C., Lee, S., … Dan, Y. (2013). Fast modulation of visual perception by basal forebrain cholinergic neurons. *Nature Publishing Group*, *16*(12), 1857–1863. https://doi.org/10.1038/nn.3552

Preston, A. R., & Eichenbaum, H. (2013). Interplay of hippocampus and prefrontal cortex in memory. *Current Biology*, *23*(17), 764–773. https://doi.org/10.1016/j.cub.2013.05.041

Rahman, J., & Berger, T. (2011). Persistent activity in layer 5 pyramidal neurons following cholinergic activation of mouse primary cortices. *European Journal of Neuroscience*, *34*(1), 22–30. https://doi.org/10.1111/j.1460-9568.2011.07736.x

Robinson, N. T. M., Priestley, J. B., Rueckemann, J. W., Garcia, A. D., Smeglin, V. A., Marino, F. A., & Eichenbaum, H. (2017). Medial Entorhinal Cortex Selectively Supports Temporal Coding by Hippocampal Neurons. *Neuron*, *94*(3), 677-688.e6. https://doi.org/10.1016/j.neuron.2017.04.003

Rotstein, H. G., Oppermann, T., White, J. A., & Kopell, N. J. (2006). The dynamic structure underlying subthreshold oscillatory activity and the onset of spikes in a model of medial entorhinal cortex stellate cells. *Journal of Computational Neuroscience*, *21*(3), 271–292. https://doi.org/10.1007/s10827-006-8096-8

Royer, S., Zemelman, B. V, Losonczy, A., Kim, J., Chance, F., Magee, J. C., & Buzsáki, G. (2012). Control of timing, rate and bursts of hippocampal place cells by dendritic and somatic inhibition. *Nature Neuroscience*, *15*(5), 769–775. https://doi.org/10.1038/nn.3077

Sabec, M. H., Wonnacott, S., Warburton, E. C., & Bashir, Z. I. (2018). Nicotinic Acetylcholine Receptors Control Encoding and Retrieval of Associative Recognition Memory through Plasticity in the Medial Prefrontal Cortex. *Cell Reports*, *22*(13), 3409–3415. https://doi.org/10.1016/j.celrep.2018.03.016

Schlesiger, M. I., Cannova, C. C., Boublil, B. L., Hales, J. B., Mankin, E. A., Brandon, M. P., … Leutgeb, S. (2015). The medial entorhinal cortex is necessary for temporal organization of hippocampal neuronal activity. *Nature Neuroscience*, *18*(8). https://doi.org/10.1038/nn.4056

Spellman, T. J., Rigotti, M., Ahmari, S. E., Fusi, S., Gogos, J. A., & Gordon, J. A. (2015). Hippocampal–prefrontal input supports spatial encoding in working memory. *Nature*, *522*(7556), 309–314. https://doi.org/10.1038/nature14445

Stokes, M. G. (2015). 'Activity-silent' working memory in prefrontal cortex: a dynamic coding framework. *Trends in Cognitive Sciences*, *19*(7), 394–405. https://doi.org/10.1016/j.tics.2015.05.004

Suh, J., Rivest, A. J., Nakashiba, T., Tominaga, T., & Tonegawa, S. (2011). Entorhinal Cortex Layer III Input to the Hippocampus Is Crucial for Temporal Association Memory. *Science*, *334*(6061), 1415–1420. https://doi.org/10.1126/science.1210125

45

Swanson, L. W., & Cowan, W. M. (1977). An Autoradiographic Study of the Organization of the Efferent Connections of the Hippocampal Formation in the Rat. *Journal of Comparative Neurology*, *172*(1), 49–84.

Takahashi, H., & Magee, J. C. (2009). Pathway Interactions and Synaptic Plasticity in the Dendritic Tuft Regions of CA1 Pyramidal Neurons. *Neuron*, *62*(1), 102–111. https://doi.org/10.1016/j.neuron.2009.03.007

Teles-Grilo Ruivo, L. M., Baker, K. L., Conway, M. W., Kinsley, P. J., Gilmour, G., Phillips, K. G., … Mellor, J. R. (2017). Coordinated Acetylcholine Release in Prefrontal Cortex and Hippocampus Is Associated with Arousal and Reward on Distinct Timescales. *Cell Reports*, *18*(4), 905–917. https://doi.org/10.1016/j.celrep.2016.12.085

Tremblay, R., Lee, S., & Rudy, B. (2016). GABAergic Interneurons in the Neocortex: From Cellular Properties to Circuits. *Neuron*, *91*(2), 260–292. https://doi.org/10.1016/j.neuron.2016.06.033

Unal, G., Joshi, A., Viney, T. J., Kis, V., & Somogyi, P. (2015). Synaptic Targets of Medial Septal Projections in the Hippocampus and Extrahippocampal Cortices of the Mouse. *Journal of Neuroscience*, *35*(48), 15812–15826. https://doi.org/10.1523/JNEUROSCI.2639-15.2015

van Strien, N. M., Cappaert, N. L. M., & Witter, M. P. (2009). The anatomy of memory: an interactive overview of the parahippocampal–hippocampal network. *Nature Reviews Neuroscience*, *10*(4), 272–282. https://doi.org/10.1038/nrn2614

Vogels, T. P., & Abbott, L. F. (2005). Signal propagation and logic gating in networks of integrate-and-fire neurons. *The Journal of Neuroscience : The Official Journal of the Society for Neuroscience*, *25*(46), 10786–10795. https://doi.org/10.1523/JNEUROSCI.3508-05.2005

Vogels, T. P., & Abbott, L. F. (2009). Gating multiple signals through detailed balance of excitation and inhibition in spiking networks. *Nature Neuroscience*, *12*(4), 483–491. https://doi.org/10.1038/nn.2276

Wang, X.-J., & Buzsáki, G. (1996). Gamma oscillation by synaptic inhibition in a hippocampal interneuronal network model. *The Journal of Neuroscience : The Official Journal of the Society for Neuroscience*, *16*(20), 6402–6413. https://doi.org/citeulike-article-id:134404

Witter, M. P., Wouterlood, F. G., Naber, P. A., & Van Haeften, T. (2000). Anatomical organization of the parahippocampal-hippocampal network. *Annals of the New York Academy of Sciences*, *911*(1), 1–24.

Wolff, M. J., Jochim, J., Akyürek, E. G., & Stokes, M. G. (2017). Dynamic hidden states underlying working-memory-guided behavior. *Nature Neuroscience*, (April). https://doi.org/10.1038/nn.4546

Womelsdorf, T., Valiante, T. a, Sahin, N. T., Miller, K. J., & Tiesinga, P. H. (2014). Dynamic circuit motifs underlying rhythmic gain control, gating and integration. *Nature Neuroscience*, *17*(8), 1031–1039. https://doi.org/10.1038/nn.3764

Wulff, P., Ponomarenko, A. a, Bartos, M., Korotkova, T. M., Fuchs, E. C., Bähner, F., … Monyer, H. (2009). Hippocampal theta rhythm and its coupling with gamma oscillations require fast inhibition onto parvalbumin-positive interneurons.

Proceedings of the National Academy of Sciences of the United States of America, *106*(9), 3561–3566. https://doi.org/10.1073/pnas.0813176106

Yamamoto, J., Suh, J., Takeuchi, D., & Tonegawa, S. (2014). Successful Execution of Working Memory Linked to Synchronized High-Frequency Gamma Oscillations. *Cell*, *157*(4), 845–857. https://doi.org/10.1016/j.cell.2014.04.009

Yang, G. R., Murray, J. D., & Wang, X. (2016). A dendritic disinhibitory circuit mechanism for pathway-specific gating. *Nature Communications*, *7*(May), 12815. https://doi.org/10.1038/ncomms12815

Zhang, H., Lin, S.-C., & Nicolelis, M. a L. (2010). Spatiotemporal coupling between hippocampal acetylcholine release and theta oscillations in vivo. *The Journal of Neuroscience*, *30*(40), 13431–13440. https://doi.org/10.1523/JNEUROSCI.1144-10.2010

Zhang, S., Xu, M., Kamigaki, T., Hoang Do, J. P., Chang, W.-C., Jenvay, S., … Dan, Y. (2014). Long-range and local circuits for top-down modulation of visual cortex processing. *Science*, *345*(6197), 660–665. https://doi.org/10.1126/science.1254126

Zheng, C., Bieri, K. W., Hsiao, Y., & Colgin, L. L. (2016). Spatial Sequence Coding Differs during Slow and Fast Gamma Rhythms in the Hippocampus. *Neuron*, *89*(2), 398–408. https://doi.org/10.1016/j.neuron.2015.12.005